Computation of energy evolution during the dynamic fracture of elastomers using the finite viscoelastic model: its implementation in Abaqus

Vasudevan Kamasamudram, Michel Coret, Nicolas Moes

COMPUTATION OF ENERGY EVOLUTION DURING THE DYNAMIC FRACTURE OF ELASTOMERS USING THE FINITE VISCOELASTIC MODEL: ITS IMPLEMENTATION IN ABAQUS

Vasudevan Kamasamudram
Nantes Université, Ecole Centrale de Nantes, CNRS, GeM, 1 rue de la Noë, 44000 Nantes, France
vasudevan.kamasamudram@ec-nantes.fr

Michel Coret
Nantes Université, Ecole Centrale de Nantes, CNRS, GeM, 1 rue de la Noë, 44000 Nantes, France
michel.coret@ec-nantes.fr

Nicolas Moës
Nantes Université, Ecole Centrale de Nantes, CNRS, GeM, 1 rue de la Noë, 44000 Nantes, France
Institut Universitaire de France, Paris, France
nicolas.moes@ec-nantes.fr

March 17, 2023

ABSTRACT

Cracks propagating in elastomers consume the strain energy available in the body through viscoelastic effects and the creation of new fracture surfaces. Determining the energy consumed by the dissipative and the fracture processes explicitly helps understand the fracture mechanisms better and if they are rate-dependent. In literature, crack propagation experiments are usually performed on thin sheets of elastomers. The displacement fields in the body as the crack propagates through it during the experiments can be accessed using the Digital Image Correlation (DIC) technique. These displacement fields can then be used as boundary conditions in finite element analysis to compute the energy evolution in the body. Using an appropriate material model to describe the bulk material, the strain energy and the viscoelastic dissipation can be computed, thereby allowing to study the energy evolution in the body as the crack passes through.

In the current study, the behavior of the elastomer material through which the crack passes has been described by the finite viscoelastic (FV) model. In such models, the viscoelastic effects are described by using some internal variables, whose evolution is prescribed through certain constitutive equations. This article first discusses the implementation of the FV model for plane stress conditions and applies it to study the dynamic fracture of elastomer membranes. The crack propagation through an elastomer is simulated by imposing the displacement fields extracted from the experiments along the crack faces onto the finite element model (thereby implicitly imposing the crack speed). The energy evolution in the body is studied to compute the energy release rate and the dissipation in the body as a consequence of viscoelastic effects. A significant portion of the energy has been observed to be consumed as the viscoelastic dissipation in the bulk material as the crack propagated.

***K*eywords** Plane stress, Finite viscoelasticity, Dynamic fracture, Elastomers

1 Introduction

Investigation of fracture of elastomers has been carried out in multiple references in history [1, 2, 3, 4]. In those studies, the crack propagation under different loading scenarios (tearing, cutting, peeling, etc.) in a specimen of elastomer was studied. The maximum crack speeds observed in [1, 3] are about $1\,\mathrm{m\,s^{-1}}$, where the experiments were conducted on the samples in tearing, cutting, and pealing configurations. In [2, 4, 5], experiments were conducted in pure shear configuration and higher crack speeds of the order of $10\,\mathrm{m\,s^{-1}}$ to $100\,\mathrm{m\,s^{-1}}$ were observed at different stretches. The inclusion of inertial effects is necessary while studying the latter cracks as the crack speeds in those cases are comparable to the elastic shear wave speeds. The inclusion of inertial effects introduces the notion of limiting speeds on the cracks (see [6] for an exhaustive review of dynamic fracture). In some fracture experiments performed on elastomers in the *pure shear* configuration in [4, 7, 8, 9] (natural rubber samples were used in [4, 7], Polyurethane in [8], and Carbon-black reinforced Styrene Butadiene Rubber (CB/SBR) was used in [9]), it was observed that the crack speeds exceeded the elastic shear wave speed of the material. These experiments are performed on a sample whose geometry is quite simple. Hence, the energy dissipated/ consumed by the cracks in the experiments is computed by simple analytical expressions, often assuming (hyper-)elastic material behavior. The values obtained can hence be considered approximate. Some studies, such as [10, 11], consider the material as viscoelastic and define an *effective tearing energy* based on the viscoelastic properties of the material. The energy left over in the body after the crack propagation was considered to compute the energy release rate in those studies. An exhaustive review of the viscoelastic fracture can be found in [12]. In that reference, the crack propagation in viscoelastic solids has been studied and expressions for the energy dissipated during the crack propagation have been obtained in terms of the *intrinsic fracture energy* and the viscoelastic properties of the material. In cases where the displacement fields in the entire body are available from the experiments, the energy consumed during the propagation of the crack can be estimated more accurately and that will be the focus of the article.

Recently, the role played by the viscoelastic effects in the bulk material during the propagation of a dynamic crack in an elastomer membrane has been investigated in [13]. Roughly, the inclusion of viscous effects introduces the notion of rubbery and glassy wave speeds depending on the modulus of the material at lower and higher strain rates. This results in a new limiting speed, allowing the crack speed to exceed the (rubbery) shear wave speed. The study in [13], however, uses a finite linear viscoelastic (FLV) model [14] to describe the behavior of the material that the crack propagates in. It is known [15] that the FLV model may not be thermodynamically consistent and also does not have expressions for the strain energy density and the dissipation functional. Hence, it is not possible to perform an energetic analysis when the FLV model is used. Also, the linearity of the evolution equations in the model restricts its application to small perturbation conditions or for *slow* processes [16]. Hence, a nonlinear finite viscoelastic (FV) model that is thermodynamically consistent has been proposed in [17, 18] and multiple other references. The FV model makes the strain energy and the energy dissipation accessible. As a consequence of the non-linearity of the model, its application is not restricted to infinitesimal perturbations - it can be applied to scenarios that are far from equilibrium. Also, the relaxation times of the viscous branches in the FV model were observed to be a function of the strain level [15]. Experiments performed on elastomers [19] also reveal the dependence of the relaxation times of the material on the strain levels and so, the FV model can be used to predict these scenarios more closely.

The FV model proposed in [18] relies on the multiplicative decomposition of the deformation gradient into elastic and viscous parts. The material was assumed to be slightly compressible and so, viscoelastic effects were included in both the volumetric and deviatoric parts of the material behavior. The details of the algorithmic treatment of the model using a mixed displacement-pressure FE method have been proposed in [20] (actually, the article describes the Bergstrom-Boyce (BB) model [21] whose viscous evolution equations can be seen as a general case of the deviatoric part of the viscous evolution equations of [18]). [22] proposes an alternative numerical treatment in the context of finite viscoelasticity and applies it to the BB model using Padé approximation to expand the exponential term resulting from using the exponential mapping technique. The numerical treatment in the case of anisotropic materials was established in [23]. Ogden model was assumed in [18] to describe the elastic and viscous branches and has also been used in [20].

The higher computational costs associated with using the mixed FE analysis can be circumvented during the analysis of thin membranes (such as the elastomer sheets used in the fracture experiments) by assuming plane stress conditions prevail. However, to the author's knowledge, the implementation of a plane stress version of the FV model does not exist. Hence, this article aims to formulate the model of [18] for plane stress conditions for the fully incompressible case and provide the details of its implementation into the `UMAT` subroutine of Abaqus [24]. It shall be noted that no changes to the model will be made as such; the model will be reformulated so that the computations of all the quantities

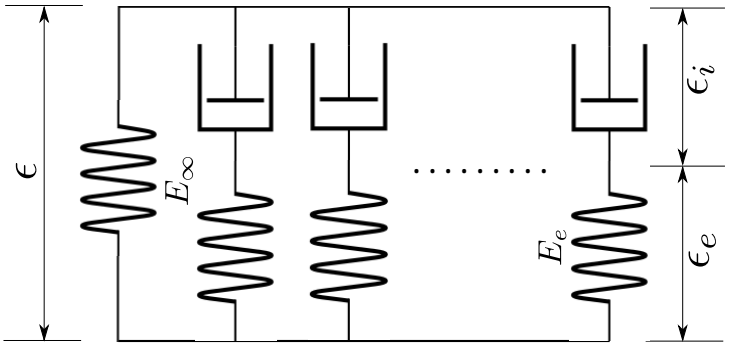

Figure 1: Generalized Maxwell model. Hyperelastic branch in parallel with multiple Maxwell viscoelastic branches.

of interest can be done by just using the in-plane component of the deformation gradient. The predictions of the FV model will be compared to the FLV model under various loading scenarios. Once this is done, the model will then be used to analyze the experiments of [8] to compute the evolution of strain energy and dissipation energy as the crack propagates through the body and to better understand the notion of Transonic cracks in elastomers. HHT-α method [25] will be used to integrate the momentum equation implicitly in time. Using the explicit time integration with the FLV model resulted in a smaller time step (of about 10^{-9} s) and hence, the implicit time integration will be used. For applications where the stable time step is not so small, the explicit time integration can be used to integrate the equations of motion, while the evolution equations for the internal variables can still be integrated implicitly using the procedure outlined in this article.

In short, the article aims to

- Establish a plane stress version of the FV model and discuss its implementation details into the `UMAT` subroutine of Abaqus.
- Compare the predictions of the FV model with those of the FLV model.
- Perform energetic analysis of the fracture experiments performed on Polyurethane elastomers.

This article proceeds as follows: first, the thermodynamics of the FV model will be described together with the evolution equations for the internal variables. Then, the plane stress formulation of the model will be presented, where the expressions for the stresses and the tangents will be obtained. The predictions of the model will then be compared to the FLV model. The model will then be used to analyze the fracture experiments performed on Polyurethane elastomer membranes.

2 The finite viscoelastic model

In this section, the basic aspects of the FV model from [18, 21] and [20] will be reviewed. Later on, the specialization of the relations between stresses and strains and the evolution equations for the plane stress scenario will be described.

2.1 Thermodynamics

Let $\phi : \mathcal{B} \rightarrow \mathcal{S}$ denote the motion of the body, where $\mathcal{B}$ and $\mathcal{S}$ are the undeformed and the deformed configurations, respectively. $\boldsymbol{x} = \phi(\boldsymbol{X}, t)$, where $\boldsymbol{x} \in \mathcal{S}$ and $\boldsymbol{X} \in \mathcal{B}$ denote the positions of a material particle in the deformed and the undeformed configurations, respectively. The deformation gradient tensor is defined as the gradient of the motion, $\boldsymbol{F} = \dfrac{\partial \phi}{\partial X}$. The determinant of the deformation gradient is denoted as J and defined as $J = \det \boldsymbol{F}$. The momentum balance equation in strong form can be expressed as

$$\operatorname{div}_0 \boldsymbol{P} = \rho_0 \boldsymbol{a}, \quad \forall \boldsymbol{x} \in \mathcal{S}, \tag{1}$$

where $\boldsymbol{P}$ denotes the nominal (PK1) stress tensor, $\boldsymbol{a}$ denotes the acceleration and ρ_0, the density of the material in the undeformed configuration.

To describe the processes that are far from equilibrium, a viscoelastic model has been proposed in [18, 21] in a thermodynamically consistent way. In this model, the strain energy density is taken to be a function of the deformation as well as some internal variables that characterize the rate dependence of the material. The strain energy density can be written as

$$\psi = \hat{\psi}(\boldsymbol{C}, \boldsymbol{Q}_1, \boldsymbol{Q}_2, ..., \boldsymbol{Q}_n), \tag{2}$$

where $\boldsymbol{C}$ is the right Cauchy Green deformation tensor, defined as $\boldsymbol{C} := \boldsymbol{F}^T\boldsymbol{F}$ and $\boldsymbol{Q}_i$ are the internal variables. The evolution of internal variables is described by n equations of the form

$$\dot{\boldsymbol{Q}}_k = \hat{\boldsymbol{f}}_k(\boldsymbol{C}, \boldsymbol{Q}_1, \boldsymbol{Q}_2, ..., \boldsymbol{Q}_n). \tag{3}$$

The evolution equations and the expression for the internal energy shall satisfy the dissipation inequality [26]

$$\mathcal{D} := \frac{1}{2}\boldsymbol{S} : \dot{\boldsymbol{C}} - \dot{\psi} \geq 0, \tag{4}$$

where $\boldsymbol{S}$ denotes the PK2 stress tensor, related to the PK1 stress as $\boldsymbol{P} = \boldsymbol{F}\boldsymbol{S}$.

Since elastomers are known to be nearly incompressible, the deformation gradient can be decomposed into volumetric and deviatoric parts. The deviatoric part of the deformation gradient can be defined as $\bar{\boldsymbol{F}} := J^{-\frac{1}{3}}\boldsymbol{F}$. The viscous response of the material is taken to be isochoric and hence, the deviatoric part of the deformation gradient is decomposed into elastic and viscous parts (Sidoroff decomposition, see [27]), $\bar{\boldsymbol{F}} = \boldsymbol{F}_e\boldsymbol{F}_i$, analogous to what is usually done in the small strain setting, see Fig. 1, where the strain in each viscous branch is decomposed into elastic (strain the spring is subjected to, ϵ_e) and viscous (strain the dashpot is subjected to, ϵ_i) parts, $\epsilon = \epsilon_e + \epsilon_i$. The variable $\boldsymbol{Q}_k$ described earlier in equation 2 can thus be identified with the viscous strain in the dashpot of the k^{th} viscous branch, $\epsilon_i^{(k)}$. This leads to the decomposition of the strain energy functional into volumetric and deviatoric parts as

$$\psi := U(J) + \hat{\psi}(\bar{\boldsymbol{F}}, \boldsymbol{F}_e). \tag{5}$$

In the above, U is the part of the strain energy functional that arises from the changes in the volume and ψ is the contribution of the deviatoric part (from both elastic and viscous branches). In the case of perfect incompressibility, $J = 1$, and the contribution of the volumetric part to the strain energy functional disappears. In such a case,

$$\psi = \hat{\psi}(\bar{\boldsymbol{F}}, \boldsymbol{F}_e). \tag{6}$$

Objectivity requirements lead the strain energy functional to depend on the right Cauchy deformation tensor. The contribution from the deviatoric part of the deformation is assumed to be further split into the contributions from the elastic (ψ_{EQ}) and viscous branches (ψ_{NEQ}) (analogous to what is usually done in small strain setting). Hence,

$$\hat{\psi} := \psi_{EQ}(\bar{\boldsymbol{C}}) + \psi_{NEQ}(\boldsymbol{C}_e), \tag{7}$$

where $\boldsymbol{C}_e$ is the elastic part of the deviatoric Cauchy Green tensor, $\boldsymbol{C}_e = \boldsymbol{F}_e^T\boldsymbol{F}_e = \boldsymbol{F}_i^{-T}\bar{\boldsymbol{C}}\boldsymbol{F}_i^{-1}$. Although the subsequent sections describe the case with one viscous branch, the case with multiple viscous branches can be described by simply writing the energy density functional as $\psi := \psi_{EQ}(\bar{\boldsymbol{C}}) + \sum_{i=1}^{N}\psi_{NEQ}^{(i)}(\boldsymbol{C}_e^{(i)})$, where $\boldsymbol{C}_e^{(i)}$ denotes the elastic strain in the i^{th} viscous branch. This corresponds to the energy split between the hyperelastic and viscoelastic branches as in Fig. 1. In this case, $\boldsymbol{Q}_k$ in equation 2 can be identified with the inverse of the viscous strain in the k^{th} viscous branch, $(\boldsymbol{C}_i^{(k)})^{-1}$ (more precisely, as $-(\boldsymbol{C}_i^{(k)})^{-1}/2$, which in small strain setting becomes $\epsilon_i^{(k)}$).

Using the above expressions in the internal dissipation inequality, equation 4, results in the expression for the stress as

$$\boldsymbol{S} = -pJ\boldsymbol{C}^{-1} + J^{-2/3}\text{DEV}\Big\{\boldsymbol{S}_{EQ} + \boldsymbol{S}_{NEQ}\Big\}. \tag{8}$$

p is the Lagrange multiplier that enforces the incompressibility constraint. $\boldsymbol{S}_{EQ}$ and $\boldsymbol{S}_{NEQ}$ denote the elastic and viscous contributions, respectively, to the total stress. $\text{DEV}\Big\{\ \bullet\ \Big\}$ represents the deviatoric projection. These stresses are given by

$$\boldsymbol{S}_{EQ} := 2\frac{\partial\psi_{EQ}}{\partial\bar{\boldsymbol{C}}}, \tag{9}$$

$$\boldsymbol{S}_{NEQ} := 2\boldsymbol{F}_i^{-1}\frac{\partial\psi_{NEQ}}{\partial\boldsymbol{C}_e}\boldsymbol{F}_i^{-T}, \tag{10}$$

and the deviatoric projector by

$$\text{DEV}\Big\{ \bullet \Big\} = \bullet - \frac{\bullet : \boldsymbol{C}}{3}\boldsymbol{C}^{-1}. \tag{11}$$

The Kirchhoff stress is then obtained as

$$\boldsymbol{\tau} = \boldsymbol{F}\boldsymbol{S}\boldsymbol{F}^T = -pJ\boldsymbol{I} + \text{dev}\big\{\boldsymbol{\tau}\big\} = -pJ\boldsymbol{I} + \mathbb{P} : \bar{\boldsymbol{\tau}}, \tag{12}$$

where $\text{dev}\big\{\boldsymbol{\tau}\big\}$ is the deviatoric part of $\boldsymbol{\tau}$ defined as $\mathbb{P} : \bar{\boldsymbol{\tau}}$ and $\boldsymbol{I}$ is the second order identity tensor. Here, $\bar{\boldsymbol{\tau}} := \bar{\boldsymbol{\tau}}_{EQ} + \bar{\boldsymbol{\tau}}_{NEQ}$ and the equilibrium and the viscous stresses are defined as

$$\bar{\boldsymbol{\tau}}_{EQ} \coloneqq 2\frac{\partial \psi_{EQ}(\bar{\boldsymbol{b}})}{\partial \bar{\boldsymbol{b}}}\bar{\boldsymbol{b}}, \tag{13}$$

$$\boldsymbol{\tau}_{NEQ} \coloneqq 2\frac{\partial \psi_{NEQ}(\boldsymbol{b}_e)}{\partial \boldsymbol{b}_e}\boldsymbol{b}_e. \tag{14}$$

$\mathbb{P}$ is the deviatoric projector in the deformed configuration defined as

$$\mathbb{P} = \mathbb{I} - \frac{\boldsymbol{I} \otimes \boldsymbol{I}}{3}, \tag{15}$$

where $\mathbb{I}$ is the fourth-order identity tensor. The remaining part of the dissipation inequality becomes

$$\mathcal{D} = -\boldsymbol{\tau}_{NEQ} : \frac{1}{2}\mathcal{L}_v\boldsymbol{b}_e \cdot \boldsymbol{b}_e^{-1} \geq 0, \tag{16}$$

where $\mathcal{L}_v\boldsymbol{b}_e$ denotes the Lie derivative of $\boldsymbol{b}_e$, defined as the push forward of the material time derivative of the pullback of $\boldsymbol{b}_e$:

$$\mathcal{L}_v\boldsymbol{b}_e = \bar{\boldsymbol{F}}\dot{\overline{\boldsymbol{C}_i^{-1}}}\bar{\boldsymbol{F}}^T. \tag{17}$$

The expression 16 can be satisfied by specifying the evolution equation as

$$-\frac{1}{2}\mathcal{L}_v\boldsymbol{b}_e \cdot \boldsymbol{b}_e^{-1} = \gamma_0\mathbb{V}^{-1} : \boldsymbol{\tau}_{NEQ}, \tag{18}$$

where $\mathbb{V}$ is a fourth-order isotropic positive definite tensor possibly a function of $\boldsymbol{b}_e$ and $\gamma_0 > 0$. A slightly different equation has been proposed by [21]. In fact, the deviatoric part of the viscous evolution equations of [18] can be seen to be a special case of that in [21]. The evolution equations for the viscous strains in [21] can be seen to be (equations 13, 17, and 24 of the reference)

$$-\frac{1}{2}\mathcal{L}_v\boldsymbol{b}_e.\boldsymbol{b}_e^{-1} = C_1(\lambda_{chain}^B - 1)^{C_2}\left(\frac{\tau_B}{\hat{\tau}_B}\right)^m \frac{1}{\sqrt{2}\tau_B}\text{dev}\Big\{\boldsymbol{\tau}\Big\}. \tag{19}$$

Taking $C_2 = 0$, and $m = 1$, equation 18 results if $C_1/(\sqrt{2}\hat{\tau}_B) = 1/(2\eta_D)$ when $\mathbb{V}^{-1} = 1/(2\eta_D)$ times the deviatoric projector.

2.2 Integration of the evolution equation

The integration of equation 18 is carried out by a predictor-corrector type algorithm as in plasticity and viscoplasticity [28], [29]. In the elastic predictor step, the inelastic strains are taken to be fixed and so,

$$(\boldsymbol{C}_i^{-1})_{tr} = (\boldsymbol{C}_i^{-1})_{t_{n-1}} \implies \boldsymbol{b}_e^{tr} = \bar{\boldsymbol{F}}(\boldsymbol{C}_i^{-1})_{t_{n-1}}\bar{\boldsymbol{F}}^T, \tag{20}$$

where the superscript *tr* refers to the value at the trial state. In the inelastic corrector step, the total deformation is assumed to be held fixed and so, $\mathcal{L}_v\boldsymbol{b}_e = \dot{\boldsymbol{b}}_e$. Using this in equation 18 gives

$$\dot{\boldsymbol{b}}_e\boldsymbol{b}_e^{-1} = -2\gamma_0\left[\mathbb{V}^{-1} : \boldsymbol{\tau}_{NEQ}\right]. \tag{21}$$

The above equation can be integrated using the exponential mapping technique [29]. The resulting expression is

$$\boldsymbol{b}_e = \exp\left[-2\gamma_0\int_{t_{n-1}}^{t_n} \mathbb{V}^{-1} : \boldsymbol{\tau}_{NEQ}\,\mathrm{d}t\right]\boldsymbol{b}_e^{tr}, \tag{22}$$

$$(\boldsymbol{b}_e)_{t_n} \approx \exp\left[-2\gamma_0 \Delta t (\mathbb{V}^{-1} : \boldsymbol{\tau}_{NEQ})_{t=t_n}\right] \boldsymbol{b}_e^{tr}. \tag{23}$$

In the above, $\Delta t = t_n - t_{n-1}$. The above equation is first order accurate.

Taking $\mathbb{V}^{-1} \coloneqq \frac{1}{2\eta_D}\mathbb{P}$, where $\mathbb{P}$ is the deviatoric projector defined in equation 15, equation 23 can be written as

$$(\boldsymbol{b}_e)_{t_n} \approx \exp\left[-\frac{\gamma_0 \Delta t}{\eta_D} \text{dev}\Big\{(\boldsymbol{\tau}_{NEQ})_{t=t_n}\Big\}\right] \boldsymbol{b}_e^{tr}. \tag{24}$$

Since the material has been assumed to be isotropic, $\boldsymbol{\tau}_{NEQ}$ and $\boldsymbol{b}_e$ share the same eigenvectors and hence commute. In such a case, equation 24 can be written as [28]

$$\boldsymbol{b}_e^{tr} = \sum_{A=1}^{3} (\lambda_{Ae})_{t_n}^2 \exp\left[\frac{\gamma_0 \Delta t}{\eta_D} (\text{dev}\big\{\tau_A\big\})_{t=t_n}\right] \boldsymbol{n}_A \otimes \boldsymbol{n}_A, \tag{25}$$

where $\boldsymbol{\tau}_{NEQ} = \sum_{A=1}^{3} \tau_A \boldsymbol{n}_A \otimes \boldsymbol{n}_A$ and $\boldsymbol{b}_e = \sum_{A=1}^{3} (\lambda_{Ae})^2 \boldsymbol{n}_A \otimes \boldsymbol{n}_A$ has been used. Comparing the above with the spectral decomposition of $\boldsymbol{b}_e^{tr}$, $\boldsymbol{b}_e^{tr} = \sum_{A=1}^{3} (\lambda_{Ae})_{tr}^2 \boldsymbol{n}_A^{tr} \otimes \boldsymbol{n}_A^{tr}$, it can be observed that eigenvectors of $\boldsymbol{b}_e^{tr}$ are same as that of $\boldsymbol{\tau}_{NEQ}$ and $\boldsymbol{b}_e$ and hence, can be computed once and for all at the beginning of a given time step. Also,

$$(\lambda_{Ae}^2)_{tr} = \exp\left[\frac{\gamma_0 \Delta t}{\eta_D} \text{dev}(\tau_A)\right] \lambda_{Ae}^2, \tag{26}$$

where the subscript $t = t_n$ has been dropped for convenience. Taking logarithm on both sides,

$$\epsilon_{Ae} = -\frac{\gamma_0 \Delta t}{2\eta_D} \text{dev}(\tau_A) + (\epsilon_{Ae})_{tr}, \tag{27}$$

where $\epsilon_{Ae} = \ln \lambda_{Ae}$ and $(\epsilon_{Ae})_{tr} = \ln(\lambda_{Ae})_{tr}$. The above equation is non-linear if τ_A is a non-linear function of ϵ_e. Hence, Newton iterations are used to solve it as below.

Defining

$$r_A \coloneqq \epsilon_{Ae} + \frac{\gamma_0 \Delta t}{2\eta_D} \text{dev}(\tau_A) - (\epsilon_{Ae})_{tr} = 0, \tag{28}$$

it can be solved by linearizing around $\epsilon_{Ae} = (\epsilon_{Ae})_k$ as

$$r_A + \frac{\partial r_A}{\partial \epsilon_{Be}} \Delta\epsilon_{Be} = 0 \implies K_{AB} \Delta\epsilon_{Be} = -r_A. \tag{29}$$

where $K_{AB} = \dfrac{\partial r_A}{\partial \epsilon_{Be}}$. The above equation is solved to obtain $\Delta\epsilon_e$, which is then used to update the elastic strain as $(\epsilon_e)_{k+1} = (\epsilon_e)_k + \Delta\epsilon_e$.

3 Plane stress formulation

As already mentioned, to the authors' knowledge, a plane stress implementation of the FV model has not been reported in the literature. This and the further sections discuss this implementation. *It shall be noted that no changes to the model will be made. Rather, all the expressions for the stresses and the tangents will be rewritten so that they can be computed using only the in-plane components of the deformation gradient ($\boldsymbol{F}$) and its elastic part ($\boldsymbol{F}_e$).*

3.1 Stress computation

In plane stress scenario and for an incompressible material, the computation of stress can be simplified. The value of p in equation 12 can be found by using the condition that $\tau_{33} = 0$. This condition can be imposed separately for the elastic and the viscous branches and the results can be combined. Since the material is assumed to be isotropic, the strain energy functional depends on the invariants, I_1 and I_2, of the strain tensor. Beginning with the elastic branch, the term $(\partial\psi/\partial\bar{\boldsymbol{b}})\bar{\boldsymbol{b}}$ can be computed as

$$\frac{\partial \psi}{\partial \bar{\boldsymbol{b}}} \bar{\boldsymbol{b}} = \left[\frac{\partial \psi}{\partial I_1} \boldsymbol{I} + \frac{\partial \psi}{\partial I_2} (I_1 \boldsymbol{I} - \boldsymbol{b})\right] \boldsymbol{b}, \tag{30}$$

where the incompressibility of the material ($J = 1$) has been taken into account. The deviatoric projection of the above term is

$$\mathbb{P} : \left(\frac{\partial \psi}{\partial \bar{\boldsymbol{b}}}\bar{\boldsymbol{b}}\right) = \left[\frac{\partial \psi}{\partial I_1}\boldsymbol{I} + \frac{\partial \psi}{\partial I_2}(I_1\boldsymbol{I} - \boldsymbol{b})\right]\boldsymbol{b} - \frac{1}{3}\left[\frac{\partial \psi}{\partial I_1}I_1 + 2\frac{\partial \psi}{\partial I_2}I_2\right]\boldsymbol{I}. \tag{31}$$

The contribution of the elastic branch to p, denoted p_e, can be written as (using $\tau_{33} = 0$ and assuming $\boldsymbol{F}$ is of the form

$$\boldsymbol{F} = \begin{bmatrix} \boldsymbol{F}_{2d} & \boldsymbol{0} \\ \boldsymbol{0}^T & F_{33} \end{bmatrix},$$

and $F_{33} = 1/\det \boldsymbol{F}^{2d}$)

$$p_e = 2\left[\frac{\partial \psi}{\partial I_1}b_{33} + \frac{\partial \psi}{\partial I_2}(I_1 b_{33} - b_{33}^2)\right] - \frac{2}{3}\left[\frac{\partial \psi}{\partial I_1}I_1 + 2\frac{\partial \psi}{\partial I_2}I_2\right]. \tag{32}$$

The total elastic part of the stress can then be found as

$$-p_e\boldsymbol{I} + 2\mathbb{P} : \left(\frac{\partial \psi}{\partial \bar{\boldsymbol{b}}}\bar{\boldsymbol{b}}\right) = 2\frac{\partial \psi}{\partial I_1}(\boldsymbol{b} - b_{33}\boldsymbol{I}) + 2\frac{\partial \psi}{\partial I_2}\left(I_1(\boldsymbol{b} - b_{33}\boldsymbol{I}) - (\boldsymbol{b}^2 - b_{33}^2\boldsymbol{I})\right). \tag{33}$$

The above equation, written with its components restricted to within the plane, can be seen to be

$$\boldsymbol{\tau}^e = 2\frac{\partial \psi}{\partial I_1}(\boldsymbol{b}^{2d} - b_{33}\boldsymbol{I}^{2d}) + 2\frac{\partial \psi}{\partial I_2}\left(I_1(\boldsymbol{b}^{2d} - b_{33}\boldsymbol{I}^{2d}) - ((\boldsymbol{b}^{2d})^2 - b_{33}^2\boldsymbol{I}^{2d})\right). \tag{34}$$

$\boldsymbol{b}^{2d}$ is the restriction of $\boldsymbol{b}$ to within the plane. As a consequence of plane stress assumption, $\boldsymbol{b}$ has been assumed to be of the form

$$\boldsymbol{b} = \begin{bmatrix} \boldsymbol{b}_{2d} & \boldsymbol{0} \\ \boldsymbol{0}^T & b_{33} \end{bmatrix},$$

where $\boldsymbol{0}$ represents the zero vector of size 2×1. Expressing the first and the second invariants in terms of in-plane components as (realizing that $b_{33} = 1/\det \boldsymbol{b}^{2d}$)

$$I_1 = \mathrm{tr}(\boldsymbol{b}^{2d}) + 1/\det(\boldsymbol{b}^{2d}), \tag{35}$$

$$I_2 = \frac{1}{2}\left[(I_1(\boldsymbol{b}^{2d}))^2 - (\boldsymbol{b}^{2d} : \boldsymbol{b}^{2d} + 1/\det(\boldsymbol{b}^{2d})^2)\right], \tag{36}$$

the term $\boldsymbol{b}^{2d} - b_{33}\boldsymbol{I}^{2d}$ in equation 34 can now be simply written as $(\partial I_1/\partial \boldsymbol{b}^{2d})\boldsymbol{b}^{2d}$ and the term $I_1(\boldsymbol{b}^{2d} - b_{33}\boldsymbol{I}^{2d}) - ((\boldsymbol{b}^{2d})^2 - b_{33}^2\boldsymbol{I}^{2d})$ as $(\partial I_2/\partial \boldsymbol{b}^{2d})\boldsymbol{b}^{2d}$. The total stress in equation 34 then simply becomes

$$\boldsymbol{\tau}^e = 2\left[\frac{\partial \psi}{\partial I_1}\frac{\partial I_1}{\partial \boldsymbol{b}^{2d}} + \frac{\partial \psi}{\partial I_2}\frac{\partial I_2}{\partial \boldsymbol{b}^{2d}}\right]\boldsymbol{b}^{2d} = 2\frac{\partial \psi}{\partial \boldsymbol{b}^{2d}}\boldsymbol{b}^{2d}. \tag{37}$$

By a similar exercise for the viscous branches, the viscous contribution to the total stress becomes

$$\boldsymbol{\tau}^v = 2\frac{\partial \psi}{\partial \boldsymbol{b}_e^{2d}}\boldsymbol{b}_e^{2d}. \tag{38}$$

Hence equations 8 and 12 become

$$\boldsymbol{\tau} = \boldsymbol{\tau}^e + \boldsymbol{\tau}^v, \quad \text{and} \tag{39}$$

$$\boldsymbol{S} = \boldsymbol{F}^{-1}\boldsymbol{\tau}\boldsymbol{F}^{-T}. \tag{40}$$

The above equations are restricted to in-plane components and the superscript $2d$ has been dropped for convenience. The total stress in equation 39 can be written for the case of multiple (say, N) viscous branches simply as $\boldsymbol{\tau} = \boldsymbol{\tau}^e + \sum_{i=1}^{N}(\boldsymbol{\tau}^v)^{(i)}$, where each of the $(\boldsymbol{\tau}^v)^{(i)}$ s now denote the viscous stress in the corresponding viscous branch, defined as

$$(\boldsymbol{\tau}^v)^{(i)} \coloneqq 2\frac{\partial \psi^{(i)}}{\partial (\boldsymbol{b}_e^{2d})^{(i)}}(\boldsymbol{b}_e^{2d})^{(i)}.$$

$(\boldsymbol{b}_e^{2d})^{(i)}$ is the left Cauchy Green tensor in the i^{th} viscous branch.

The two invariants written in terms of principal stretches become

$$I_1 = \lambda_A^2 + \lambda_B^2 + \lambda_C^2 = \lambda_A^2 + \lambda_B^2 + 1/\lambda_A^2\lambda_B^2, \tag{41}$$

$$I_2 = \lambda_A^2\lambda_B^2 + \lambda_B^2\lambda_C^2 + \lambda_C^2\lambda_A^2 = \lambda_A^2\lambda_B^2 + 1/\lambda_A^2 + 1/\lambda_B^2, \tag{42}$$

where $\lambda_C^2 = 1/\lambda_A^2\lambda_B^2$ has been used.

Using the above, the Kirchhoff stress can be written in principal basis to be

$$\tau_A = 2\lambda_A^2 \frac{\partial \psi}{\partial \lambda_A^2} = 2\lambda_A^2 \left[\frac{\partial \psi}{\partial I_1}\frac{\partial I_1}{\partial \lambda_A^2} + \frac{\partial \psi}{\partial I_2}\frac{\partial I_2}{\partial \lambda_A^2} \right], \tag{43}$$

$$\tau_B = 2\lambda_B^2 \frac{\partial \psi}{\partial \lambda_B^2} = 2\lambda_B^2 \left[\frac{\partial \psi}{\partial I_1}\frac{\partial I_1}{\partial \lambda_B^2} + \frac{\partial \psi}{\partial I_2}\frac{\partial I_2}{\partial \lambda_B^2} \right], \tag{44}$$

and $\tau_C = 0$ as a consequence of the plane stress assumption. The partial derivatives of the invariants can be evaluated as

$$\frac{\partial I_1}{\partial \lambda_A^2} = 1 - 1/\lambda_A^4\lambda_B^2, \quad \frac{\partial I_1}{\partial \lambda_B^2} = 1 - 1/\lambda_A^2\lambda_B^4, \tag{45}$$

$$\frac{\partial I_2}{\partial \lambda_A^2} = \lambda_B^2 - 1/\lambda_A^4, \quad \frac{\partial I_2}{\partial \lambda_B^2} = \lambda_A^2 - 1/\lambda_B^4. \tag{46}$$

The stresses can be expressed in global Cartesian basis by using

$$\boldsymbol{\tau} = \tau_1 \boldsymbol{n}_1 \otimes \boldsymbol{n}_1 + \tau_2 \boldsymbol{n}_2 \otimes \boldsymbol{n}_2, \tag{47}$$

where $\boldsymbol{n}_1$ and $\boldsymbol{n}_2$ are the eigenvectors of $\boldsymbol{b} = \boldsymbol{F}\boldsymbol{F}^T$. As a recollection, the stresses obtained this way are the total stresses, $\boldsymbol{\tau} = -pJ\boldsymbol{I} + \boldsymbol{\tau}^{iso} = -pJ\boldsymbol{I} + \mathbb{P} : \bar{\boldsymbol{\tau}}$.

Stresses can be similarly computed in viscous branches where λ is replaced by λ_e, which are the eigen values of $\boldsymbol{b}_e = \boldsymbol{F}_e\boldsymbol{F}_e^T$, $\boldsymbol{n}_i$s replaced by $(\boldsymbol{n}_i)_e$s, the eigenvectors of $\boldsymbol{b}_e$ and the ψ replaced by the strain energy of the corresponding viscous branch.

3.2 Integration of evolution equation

For viscous branches, the evolution equations remain the same even in the plane stress scenario. The residual can be written, similar to equation 28 as

$$r_A = \epsilon_{Ae} + \frac{\gamma_0 \Delta t}{2\eta_D}\text{dev}(\tau_A) - (\epsilon_{Ae})_{tr} = 0, \tag{48}$$

Since plane stress condition is assumed to prevail, only the in-plane components of the above equation are considered. Also, the deviatoric part of the Kirchhoff stress can be expressed as $\text{dev}(\boldsymbol{\tau}) = \boldsymbol{\tau} + p\boldsymbol{I}$, where p is the Lagrange multiplier that enforces incompressibility, which is found by using the condition that $\tau_3 = 0$. $\boldsymbol{\tau}$ can be evaluated by using the procedure in the previous section. The expression for p can be seen to be

$$p = -\frac{\tau_1 + \tau_2}{3}. \tag{49}$$

The above equation can be obtained by taking the trace of equation 12 and realizing that $\tau_3 = 0$ as a consequence of plane stress assumption and that trace of the deviatoric projector is 0. The in-plane evolution equations then become

$$r_1 = \epsilon_{1e} + \frac{\gamma_0 \Delta t}{2\eta_D}(\tau_1 + p) - (\epsilon_{1e})_{tr} = 0, \tag{50}$$

$$r_2 = \epsilon_{2e} + \frac{\gamma_0 \Delta t}{2\eta_D}(\tau_2 + p) - (\epsilon_{2e})_{tr} = 0. \tag{51}$$

In the third direction, the evolution equation becomes $\epsilon_{3e} + \frac{\gamma_0 \Delta t}{2\eta_D}p - (\epsilon_{3e})_{tr} = 0$. It can be shown that solving the first two equations will result in the third equation being satisfied automatically. Adding equations 50 and 51 will result in $\epsilon_{1e} + \epsilon_{2e} + \frac{\gamma_0 \Delta t}{2\eta_D}(\tau_1 + \tau_2 + 2p) - [(\epsilon_{1e})_{tr} + (\epsilon_{2e})_{tr}] = 0$. This, in conjunction with the assumption of incompressibility and plane stress condition, results in $\epsilon_{3e} + \frac{\gamma_0 \Delta t}{2\eta_D}p - (\epsilon_{3e})_{tr} = 0$, which is the third equation.

Equations 50 and 51 are solved iteratively using the Newton method.

$$r_A^{(k+1)} = r_A^{(k)} + \frac{\partial r_A}{\partial \epsilon_{Be}}\Delta\epsilon_{Be} = 0. \tag{52}$$

This in turn requires the evaluation of $K_{AB} = \dfrac{\partial r_A}{\partial \epsilon_{Be}}$. This can be evaluated as

$$K_{AB} = \frac{\partial r_A}{\partial \epsilon_{Be}} = \delta_{AB} + \frac{\gamma_0 \Delta t}{2\eta_D}\left(\frac{\partial \tau_A}{\partial \epsilon_{Be}} + \frac{\partial p}{\partial \epsilon_{Be}}\right). \tag{53}$$

The pressure derivative can be computed from equation 49 as

$$\frac{\partial p}{\partial \epsilon_{Ae}} = -\frac{1}{3}\left(\frac{\partial \tau_1}{\partial \epsilon_{Ae}} + \frac{\partial \tau_2}{\partial \epsilon_{Ae}}\right). \tag{54}$$

The computation of derivative $\dfrac{\partial \tau_A}{\partial \epsilon_{Be}}$ can be carried out as shown in the following sections.

3.3 Tangent computation

Integrating the momentum equations using implicit time integration schemes requires the calculation of the tangent. The tangent for the elastic branch can be computed using the value of the current deformation gradient and in the case of viscous branches, the tangent calculation is slightly more involved. The next section addresses the calculation of the tangent for the elastic branch while the calculation for viscous branches will be carried out thereafter.

3.3.1 For elastic branch

The calculation of tangent proceeds in a similar way to that of the 3D case [30]. It first involves the calculation of $\mathfrak{C} = 2\dfrac{\partial \boldsymbol{S}}{\partial \boldsymbol{C}}$. The derivative can be calculated by noting that [30, 31]

$$\dot{\boldsymbol{S}} = \frac{\partial \boldsymbol{S}}{\partial \boldsymbol{C}} : \dot{\boldsymbol{C}}. \tag{55}$$

Since $\boldsymbol{C} = \sum_{i=1}^{2} \lambda_i^2 \boldsymbol{N}_i \otimes \boldsymbol{N}_i$, $\dot{\boldsymbol{C}} = \sum_{i=1}^{2}\left[\dfrac{\partial \lambda_i^2}{\partial t}\boldsymbol{N}_i \otimes \boldsymbol{N}_i + \lambda_i^2 \dot{\boldsymbol{N}}_i \otimes \boldsymbol{N}_i + \lambda_i^2 \boldsymbol{N}_i \otimes \dot{\boldsymbol{N}}_i\right]$. $\dot{\boldsymbol{N}}_i = \sum_{j=1}^{2} W_{ij}\boldsymbol{N}_j$, where $W_{ij} = -W_{ji}$ are the components of a skew symmetric tensor. Hence

$$\dot{\boldsymbol{C}} = \sum_{i=1}^{2} \frac{\partial \lambda_i^2}{\partial t}\boldsymbol{N}_i \otimes \boldsymbol{N}_i + \sum_{i,j=1, i\neq j}^{2} W_{ij}(\lambda_i^2 - \lambda_j^2)\boldsymbol{N}_i \otimes \boldsymbol{N}_j. \tag{56}$$

As a consequence of isotropy, $\boldsymbol{S}$ and $\boldsymbol{C}$ share the eigenvectors. Hence, following the same procedure,

$$\dot{\boldsymbol{S}} = \sum_{i,j=1}^{2} 2\frac{\partial^2 \psi}{\partial \lambda_i^2 \partial \lambda_j^2}\frac{\partial \lambda_j^2}{\partial t}\boldsymbol{N}_i \otimes \boldsymbol{N}_i + \sum_{i,j=1, i\neq j}^{2} W_{ij}(S_i - S_j)\boldsymbol{N}_i \otimes \boldsymbol{N}_j. \tag{57}$$

The tangent can hence be written as

$$\mathfrak{C} = \sum_{i,j=1}^{2} 4\frac{\partial^2 \psi}{\partial \lambda_i^2 \partial \lambda_j^2}\boldsymbol{N}_i \otimes \boldsymbol{N}_i \otimes \boldsymbol{N}_j \otimes \boldsymbol{N}_j + \sum_{i,j=1, i\neq j}^{2} \frac{S_i - S_j}{\lambda_i^2 - \lambda_j^2}(\boldsymbol{N}_i \otimes \boldsymbol{N}_j \otimes \boldsymbol{N}_i \otimes \boldsymbol{N}_j + \boldsymbol{N}_i \otimes \boldsymbol{N}_j \otimes \boldsymbol{N}_j \otimes \boldsymbol{N}_i). \tag{58}$$

Its push forward to the spatial configuration, $\mathfrak{c}_{ijkl} = 2F_{iI}F_{jJ}F_{kK}F_{lL}\dfrac{\partial S_{IJ}}{\partial C_{KL}}$, can be seen to be

$$\mathfrak{c} = \sum_{i,j=1}^{2} (C_{ij} - 2\sigma_i \delta_{ij})\boldsymbol{n}_i \otimes \boldsymbol{n}_i \otimes \boldsymbol{n}_j \otimes \boldsymbol{n}_j + \sum_{i,j=1, i\neq j}^{2} \frac{\sigma_i \lambda_j^2 - \sigma_j \lambda_i^2}{\lambda_i^2 - \lambda_j^2}(\boldsymbol{n}_i \otimes \boldsymbol{n}_j \otimes \boldsymbol{n}_i \otimes \boldsymbol{n}_j + \boldsymbol{n}_i \otimes \boldsymbol{n}_j \otimes \boldsymbol{n}_j \otimes \boldsymbol{n}_i), \tag{59}$$

where $C_{ij} = \dfrac{\partial^2 \psi}{\partial \ln \lambda_i \partial \ln \lambda_j} = \dfrac{\partial \tau_i}{\partial \epsilon_j}$ and $\sigma_i = \tau_i$, since the material is incompressible. The components of the above fourth order tensor can be stored in a matrix as

$$[\mathfrak{c}] = \begin{bmatrix} C_{1111} & C_{1122} & C_{1112} \\ C_{2211} & C_{2222} & C_{2212} \\ C_{1211} & C_{1222} & C_{1212} \end{bmatrix}_{(\boldsymbol{n}_1, \boldsymbol{n}_2)}. \tag{60}$$

The components of the tangent can be converted to Cartesian basis by using the transformation [32]

$$[\mathfrak{c}]_{(\boldsymbol{e}_1,\boldsymbol{e}_2)} = [P][\mathfrak{c}]_{(\boldsymbol{n}_1,\boldsymbol{n}_2)}[P]^T, \tag{61}$$

where

$$[P] = \begin{bmatrix} Q_{11}^2 & Q_{12}^2 & 2Q_{11}Q_{12} \\ Q_{21}^2 & Q_{22}^2 & 2Q_{21}Q_{22} \\ Q_{11}Q_{21} & Q_{12}Q_{22} & Q_{11}Q_{22}+Q_{12}Q_{21} \end{bmatrix}. \tag{62}$$

Here, Q_{ij}s are the elements of $[Q]$ matrix which is the transpose of $[\tilde{Q}]$, $[Q] = [\tilde{Q}]^T$. The columns of $[\tilde{Q}]$ matrix are the components of eigenvectors of $\boldsymbol{b}$ in cartesian basis.

The calculation of $\mathfrak{c}$ requires the calculation of $\dfrac{\partial \tau_i}{\partial \epsilon_j}$, which can be carried out as follows

$$\frac{\partial \tau_i}{\partial \epsilon_j} = 2\lambda_j^2 \frac{\partial \tau_i}{\partial \lambda_j^2}, \quad \text{i,j=1,2.} \tag{63}$$

$$\frac{\partial \tau_i}{\partial \lambda_j^2} = 2\left[\frac{\partial^2 \psi}{\partial \lambda_j^2 \partial I_1}\lambda_i^2 \frac{\partial I_1}{\partial \lambda_i^2} + \frac{\partial \psi}{\partial I_1}\frac{\partial}{\partial \lambda_j^2}\left(\lambda_i^2 \frac{\partial I_1}{\partial \lambda_i^2}\right) + \frac{\partial^2 \psi}{\partial \lambda_j^2 \partial I_2}\lambda_i^2 \frac{\partial I_2}{\partial \lambda_i^2} + \frac{\partial \psi}{\partial I_2}\frac{\partial}{\partial \lambda_j^2}\left(\lambda_i^2 \frac{\partial I_2}{\partial \lambda_i^2}\right)\right]. \tag{64}$$

The partial derivatives can be further evaluated as

$$\frac{\partial^2 \psi}{\partial \lambda_i^2 \partial I_j} = \frac{\partial^2 \psi}{\partial I_1 \partial I_j}\frac{\partial I_1}{\partial \lambda_i^2} + \frac{\partial^2 \psi}{\partial I_2 \partial I_j}\frac{\partial I_2}{\partial \lambda_i^2} \tag{65}$$

$$\frac{\partial}{\partial \lambda_A^2}\left(\lambda_A^2 \frac{\partial I_1}{\partial \lambda_A^2}\right) = 1 + 1/\lambda_A^4\lambda_B^2, \quad \frac{\partial}{\partial \lambda_B^2}\left(\lambda_A^2 \frac{\partial I_1}{\partial \lambda_A^2}\right) = 1/\lambda_A^2\lambda_B^4, \tag{66}$$

$$\frac{\partial}{\partial \lambda_A^2}\left(\lambda_A^2 \frac{\partial I_2}{\partial \lambda_A^2}\right) = \lambda_B^2 + 1/\lambda_A^4, \quad \frac{\partial}{\partial \lambda_B^2}\left(\lambda_A^2 \frac{\partial I_2}{\partial \lambda_A^2}\right) = \lambda_A^2. \tag{67}$$

Remark. *The total stress and tangent calculation in the case of plane stress condition for incompressible materials involves the calculation of derivatives* ***after*** *enforcing all the material (incompressibility) and geometric (plane stress) constraints.*

In case of equal eigen values $\lambda_1 = \lambda_2$, the second term of equation 59 takes a $\frac{0}{0}$ form and so, L'Hospital's rule is used to compute it.

$$\lim_{\lambda_2 \to \lambda_1} \frac{\sigma_1\lambda_2^2 - \sigma_2\lambda_1^2}{\lambda_1^2 - \lambda_2^2} = \frac{1}{2}\left[\frac{\partial^2 \psi}{\partial \epsilon_2 \partial \epsilon_2} - \frac{\partial^2 \psi}{\partial \epsilon_1 \partial \epsilon_2}\right] - \sigma_2 = \frac{1}{2}\left[\frac{\partial \tau_2}{\partial \epsilon_2} - \frac{\partial \tau_2}{\partial \epsilon_1}\right] - \tau_2. \tag{68}$$

Jaumann rate of Kirchhoff stress

Recalling equation 55,

$$\dot{\boldsymbol{S}} = \frac{\partial \boldsymbol{S}}{\partial \boldsymbol{C}} : \dot{\boldsymbol{C}}. \tag{55}$$

Now, using the relation between the stresses as $\boldsymbol{\tau} = \boldsymbol{F}\boldsymbol{S}\boldsymbol{F}^T$ and its time derivative, $\dot{\boldsymbol{\tau}} = \boldsymbol{F}\dot{\boldsymbol{S}}\boldsymbol{F}^T + \dot{\boldsymbol{F}}\boldsymbol{S}\boldsymbol{F}^T + \boldsymbol{F}\boldsymbol{S}\dot{\boldsymbol{F}}^T$, equation 55 can be rewritten as

$$\dot{\boldsymbol{\tau}} - \boldsymbol{l}\boldsymbol{\tau} - \boldsymbol{\tau}\boldsymbol{l}^T = \boldsymbol{F}\left(\frac{\partial \boldsymbol{S}}{\partial \boldsymbol{C}} : \dot{\boldsymbol{C}}\right)\boldsymbol{F}^T, \tag{69}$$

where $\boldsymbol{l} = \dot{\boldsymbol{F}}\boldsymbol{F}^{-1}$ has been used. Now, using $\boldsymbol{l} = \boldsymbol{d} + \boldsymbol{W}$, where $\boldsymbol{d}$ and $\boldsymbol{W}$ are the symmetric and skew-symmetric parts of $\boldsymbol{l}$, respectively, the above equation becomes

$$\dot{\boldsymbol{\tau}} - \boldsymbol{W}\boldsymbol{\tau} + \boldsymbol{\tau}\boldsymbol{W} = \boldsymbol{F}\left(\frac{\partial \boldsymbol{S}}{\partial \boldsymbol{C}} : \dot{\boldsymbol{C}}\right)\boldsymbol{F}^T + \boldsymbol{d}\boldsymbol{\tau} + \boldsymbol{\tau}\boldsymbol{d}, \tag{70}$$

where $\boldsymbol{W}^T = -\boldsymbol{W}$ and $\boldsymbol{d}^T = \boldsymbol{d}$ has been used.

The tangent to be supplied to Abaqus corresponds to the Jaumann rate of the Kirchhoff stress ($\mathcal{C}^{(JK)}$) written as [33]

$$\overset{\nabla}{\boldsymbol{\tau}}{}^{(JK)} = \dot{\boldsymbol{\tau}} + \boldsymbol{\tau}\boldsymbol{W} - \boldsymbol{W}\boldsymbol{\tau} = \mathcal{C}^{(JK)} : \boldsymbol{d}. \tag{71}$$

$\mathcal{C}^{(JK)}$ can hence be seen to be related to $\mathfrak{c}$ as (by writing equation 70 in component form)

$$\mathcal{C}_{ijkl}^{(JK)} = \mathfrak{c}_{ijkl} + \frac{1}{2}(\sigma_{ij}\delta_{kl} + \sigma_{kl}\delta_{ij} + \sigma_{il}\delta_{jk} + \sigma_{jk}\delta_{il}). \tag{72}$$

3.3.2 For viscous branches

For the viscous branches, the following procedure will be used to calculate the tangent similar to the case of plasticity as in [28, 34] and to the case of viscoelasticity as in [18]. All the stress and strain components are now restricted to the plane.

Beginning as in the case of the elastic branch, the calculation of tangent involves the calculation of the derivative of PK-2 stress with respect to the Cauchy Green tensor (see equation 55). The stresses in the viscous branches are a function of the corresponding $\boldsymbol{b}_e$ and hence, ϵ_e. Equation 27 defines an implicit relation between ϵ_e and the $(\epsilon_e)_{tr}$ and hence, the stresses in the viscous branches can be seen to depend implicitly on $(\epsilon_e)_{tr}$. The trial state of elastic strain is computed from the current state of total deformation and the inelastic strain at the previous step ($\boldsymbol{b}_e^{tr} = \boldsymbol{F}^n(\boldsymbol{C}_i^{n-1})^{-1}(\boldsymbol{F}^n)^T$) and hence, does not change during a given time step when equation 27 is being solved. Hence, the trial elastic state can be seen as a function of the total deformation (only). The tangent can hence be computed by the repeated use of the chain rule.

As a first step, since in the elastic trial state, the inelastic strain is held fixed, $\boldsymbol{F}^n = \boldsymbol{F}_e^{tr}\boldsymbol{F}_i^{n-1}$. Hence, $\boldsymbol{C}^n = (\boldsymbol{F}_i^{n-1})^T\boldsymbol{C}_e^{tr}\boldsymbol{F}_i^{n-1}$. In this step, the chain rule can be used to convert the derivative from with respect to $\boldsymbol{C}$ to with respect to $\boldsymbol{C}_e^{tr}$.

$$\frac{\partial S_{IJ}}{\partial C_{KL}} = \frac{\partial S_{IJ}}{\partial (C_e^{tr})_{\alpha\beta}}\frac{\partial (C_e^{tr})_{\alpha\beta}}{\partial C_{KL}} = \left((\boldsymbol{F}_i^{n-1})^{-1}\right)_{K\alpha}\left((\boldsymbol{F}_i^{n-1})^{-1}\right)_{L\beta}\frac{\partial S_{IJ}}{\partial (C_e^{tr})_{\alpha\beta}}, \tag{73}$$

where the symmetry of $\boldsymbol{C}_e^{tr}$ has been used. $\boldsymbol{F}_i^{n-1}$ is a constant at the current time step.

Since in viscous branches,

$$\boldsymbol{S} = \boldsymbol{F}^{-1}\boldsymbol{\tau}\boldsymbol{F}^{-T} = (\boldsymbol{F}_i^{n-1})^{-1}.\underbrace{(\boldsymbol{F}_e^{tr})^{-1}\boldsymbol{\tau}(\boldsymbol{F}_e^{tr})^{-T}}_{\tilde{\boldsymbol{S}}}.(\boldsymbol{F}_i^{n-1})^{-T}, \tag{74}$$

the stress derivative can be further refined as

$$\frac{\partial S_{IJ}}{\partial (C_e^{tr})_{\alpha\beta}} = \left((\boldsymbol{F}_i^{n-1})^{-1}\right)_{I\gamma}\left((\boldsymbol{F}_i^{n-1})^{-1}\right)_{J\delta}\frac{\partial \tilde{S}_{\gamma\delta}}{\partial (C_e^{tr})_{\alpha\beta}}. \tag{75}$$

Hence,

$$2\frac{\partial S_{IJ}}{\partial C_{KL}} = 2\left((\boldsymbol{F}_i^{n-1})^{-1}\right)_{I\gamma}\left((\boldsymbol{F}_i^{n-1})^{-1}\right)_{J\delta}\left((\boldsymbol{F}_i^{n-1})^{-1}\right)_{K\alpha}\left((\boldsymbol{F}_i^{n-1})^{-1}\right)_{L\beta}\frac{\partial \tilde{S}_{\gamma\delta}}{\partial (C_e^{tr})_{\alpha\beta}}. \tag{76}$$

The push-forward of above by $\boldsymbol{F}$ results in

$$\mathfrak{c}_{ijkl} = 2F_{iI}F_{jJ}F_{kK}F_{lL}\frac{\partial S_{IJ}}{\partial C_{KL}} = 2(\boldsymbol{F}_e^{tr})_{i\gamma}(\boldsymbol{F}_e^{tr})_{j\delta}(\boldsymbol{F}_e^{tr})_{k\alpha}(\boldsymbol{F}_e^{tr})_{l\beta}\frac{\partial \tilde{S}_{\gamma\delta}}{\partial (C_e^{tr})_{\alpha\beta}}. \tag{77}$$

Expressing $\boldsymbol{F}_e^{tr}$ as $\boldsymbol{F}_e^{tr} = \sum_{A=1}^3(\lambda_{Ae})_{tr}\boldsymbol{n}_A \otimes \tilde{\boldsymbol{N}}_A$, $(\boldsymbol{F}_e^{tr})^{-1} = \sum_{A=1}^3 \frac{1}{(\lambda_{Ae})_{tr}}\tilde{\boldsymbol{N}}_A \otimes \boldsymbol{n}_A$ and $(\boldsymbol{F}_e^{tr})^{-T} = \sum_{A=1}^3 \frac{1}{(\lambda_{Ae})_{tr}}\boldsymbol{n}_A \otimes \tilde{\boldsymbol{N}}_A$. $\tilde{\boldsymbol{S}}$ can hence be written as

$$\tilde{\boldsymbol{S}} = \sum_{A=1}^{2}\frac{\tau_A}{(\lambda_{Ae})_{tr}^2}\tilde{\boldsymbol{N}}_A \otimes \tilde{\boldsymbol{N}}_A. \tag{78}$$

Also, $\boldsymbol{C}_e^{tr} = \sum_{A=1}^3(\lambda_{Ae})_{tr}^2\tilde{\boldsymbol{N}}_A \otimes \tilde{\boldsymbol{N}}_A$. It is to be noted that the τ_A in the above equation is a function of ϵ_e. The development from here is similar to that used to arrive at equation 59 except that C_{ij} in that equation will be replaced by C_{ij}^{alg}, which will be defined below. Using the fact that $\boldsymbol{F}_e^{tr}\tilde{\boldsymbol{N}}_A = (\lambda_{Ae})_{tr}\boldsymbol{n}_A$, the expression for the tangent can be seen to be

$$\mathfrak{c} = \sum_{i,j=1}^{2}(C_{ij}^{alg} - 2\sigma_i\delta_{ij})\boldsymbol{n}_i\otimes\boldsymbol{n}_i\otimes\boldsymbol{n}_j\otimes\boldsymbol{n}_j + \sum_{i,j=1,i\neq j}^{2}\frac{\sigma_i(\lambda_j)_{tr}^2 - \sigma_j(\lambda_i)_{tr}^2}{(\lambda_i)_{tr}^2 - (\lambda_j)_{tr}^2}(\boldsymbol{n}_i\otimes\boldsymbol{n}_j\otimes\boldsymbol{n}_i\otimes\boldsymbol{n}_j + \boldsymbol{n}_i\otimes\boldsymbol{n}_j\otimes\boldsymbol{n}_j\otimes\boldsymbol{n}_i). \tag{79}$$

In the above, $C_{AC}^{alg} = \frac{\partial \tau_A}{\partial (\epsilon_{Ce})_{tr}}$. Since τ_As are a function of ϵ_es, the derivative is computed using the chain rule.

$$\frac{\partial \tau_A}{\partial (\epsilon_{Ce})_{tr}} = \frac{\partial \tau_A}{\partial \epsilon_{Be}}\frac{\partial \epsilon_{Be}}{\partial (\epsilon_{Ce})_{tr}}. \tag{80}$$

The derivative $\dfrac{\partial \epsilon_{Be}}{\partial (\epsilon_{Ce})_{tr}}$ can be computed by realizing that equations $r_B = 0$ are satisfied at the end of local Newton iterations and hence are valid at all the times during the global Newton iterations. Hence, during the global Newton iterations, $\dfrac{\partial r_B}{\partial (\epsilon_{Ce})_{tr}} = 0$ as well. Hence,

$$\frac{\partial \epsilon_{Be}}{\partial (\epsilon_{Ce})_{tr}} = K_{BC}^{-1}, \tag{81}$$

where K_{BC} is defined in equation 53.

The expression for dissipation becomes

$$\mathcal{D} = \frac{1}{2\eta_D} \text{dev}\{\boldsymbol{\tau}_{NEQ}\} : \text{dev}\{\boldsymbol{\tau}_{NEQ}\} = \frac{1}{2\eta_D} \left[(\boldsymbol{\tau} + p\boldsymbol{I}) : (\boldsymbol{\tau} + p\boldsymbol{I}) + p^2 \right], \tag{82}$$

which can be seen to be positive since $\eta_D > 0$. In the above equation, $\boldsymbol{\tau}$ is as evaluated in equation 47.

4 Description of the implementation

The plane stress version of the model described above has been implemented into the `UMAT` subroutine of Abaqus. The subroutine computes the stress and tangent for a given time step and also updates the internal variables. The implementation details will be discussed in this section.

Algorithm 1: Steps followed in `UMAT` for the plane stress FV model

Data: $\boldsymbol{F}^n$, $\boldsymbol{C}_i^{n-1}$, Δt
Result: $\boldsymbol{\tau}^n$, $\boldsymbol{C}_i^n$, $C^{(\mathcal{GK})}$, ψ^n, $\mathcal{D}^n$
$(\boldsymbol{b}_e)_{tr} = \boldsymbol{F}^n (\boldsymbol{C}_i^{n-1})^{-1} (\boldsymbol{F}^n)^T$;
Compute $(\lambda_e)_{tr}$ and $\boldsymbol{n}_A$ so that $(\boldsymbol{b}_e)_{tr} = \sum_{A=1}^{2} (\lambda_{Ae})_{tr}^2 \boldsymbol{n}_A \otimes \boldsymbol{n}_A$;
Compute $(\epsilon_{Ae})_{tr} = \ln((\lambda_{Ae})_{tr})$;
$k = 0$, $\epsilon_{Ae} \leftarrow (\epsilon_{Ae})_{tr}$;
do
  Compute $\boldsymbol{\tau}$ and p from ϵ_{Ae};
  $r_A :- \epsilon_{Ae} + \frac{\Delta t}{2\eta}(\tau_A + p) - (\epsilon_{Ae})_{tr} = 0$;
  Compute $\dfrac{\partial \tau_A}{\partial \epsilon_{Be}}$, $\dfrac{\partial p}{\partial \epsilon_{Be}}$;
  $K_{AB} = \delta_{AB} + \frac{\Delta t}{22.\eta} \left(\dfrac{\partial \tau_A}{\partial \epsilon_{Be}} + \dfrac{\partial p}{\partial \epsilon_{Be}} \right)$;
  $\Delta \epsilon_{Ae}^k = -K_{AB}^{-1} r_A$;
  $\epsilon_{Ae}^{k+1} \leftarrow \epsilon_{Ae}^k + \Delta \epsilon_{Ae}^k$;
  $k \leftarrow k + 1$
while $||r_A|| > TOL$;
Update $\boldsymbol{\tau}^n$, p, $\lambda_{Ae} = \exp(\epsilon_{Ae})$, and K_{AB};
$\boldsymbol{b}_e = \sum_{A=1}^{2} \lambda_{Ae}^2 \boldsymbol{n}_A \otimes \boldsymbol{n}_A$, $\boldsymbol{b}_e^{-1} = \sum_{A=1}^{2} \lambda_{Ae}^{-2} \boldsymbol{n}_A \otimes \boldsymbol{n}_A$;
$\boldsymbol{C}_i^n = (\boldsymbol{F}^n)^T \boldsymbol{b}_e^{-1} \boldsymbol{F}^n$;
Compute $C^{(\mathcal{GK})}$using C^{alg}, τ_A, and λ_{Ae};
Compute $\psi^n$and $\mathcal{D}^n$;

The working of the subroutine can be seen in algorithm 1. The superscript n indicates the quantity at the current time and $n-1$ indicates the quantity at the previous time. Δt is defined as the time increment size, $t_n - t_{n-1}$. As can be seen, the internal variables are updated and the strain energy density and dissipation are computed with the updated values of $\boldsymbol{b}_e$ and $\boldsymbol{\tau}$. The value of TOL has been chosen to be 10^{-5}. The `C++` implementation of the model can be found at [35]. The list of arrays that contain the inputs to the subroutine and the arrays into which the outputs will be written can be found in table 1.

```
void FOR_NAME(umat)(double* STRESS, double* STATEV, double* DDSDDE, ... ,double*
TIME, double* DTIME, ... , double* DFGRD0, double* DFGRD1, ... )
```

Table 1: Variables and arrays that provide the input and obtain the outputs from the subroutine.

Variable	Name of the array	Description
$\boldsymbol{F}$	DFGRD1	Deformation gradient $F_{xx}, F_{yx}, F_{xy}, F_{yy}$
$\boldsymbol{\tau}$	STRESS	Cauchy stress $\tau_{xx}, \tau_{yy}, \tau_{xy}$
$\mathcal{C}^{(JK)}$	DDSDDE	Jaumann rate of Kirchhoff stress
$(\boldsymbol{C}^i)^a - \boldsymbol{I}$	STATEV #$(5a-4)$ to STATEV #$(5a-1)$	Inelastic Cauchy Green tensor (difference the Identity tensor) in the ath viscous branch. $(C^i)^a_{xx} - 1$ in STATEV #$(5a-4)$, $(C^i)^a_{xy}$ in STATEV #$(5a-3)$, $(C^i)^a_{xy}$ in STATEV #$(5a-2)$, $(C^i)^a_{yy} - 1$ in STATEV #$(5a-1)$
ψ^a/ψ^∞	STATEV #$5a$	Ratio of the strain energy in the ath viscous branch to the strain energy in the hyperelastic branch
$\psi^\infty + \sum_{i=1}^{N} \psi_i$	SSE	Total strain energy
D	SCD	Energy dissipated

A rough flow of control in the subroutine can be seen in Fig. 2. The implementation has been distributed between the two classes, `spring` and `dashpot`. The two classes are precompiled to create a static library `libusublib.a`, which is then linked to Abaqus. The model for the spring in the viscous branch can be chosen arbitrarily. Currently, a Polynomial model has been used.

The deformation gradient (in the `DFGRD1` array) and the internal variables ($\boldsymbol{C}_i$) at the beginning of the step (in the `STATEV` array) are obtained as an input to the subroutine from Abaqus. The values of the $\boldsymbol{C}_i$ at the previous time step can be used to compute $\boldsymbol{b}_e^{tr}$ using equation 20 as in line 1 of the algorithm. The Eigenvalues and the Eigenvectors of $\boldsymbol{b}_e^{tr}$ are then computed (line 2 of the algorithm). The components of the Eigenvectors are then used to compute the matrix (see equation 62) that is used to change the basis (of the tangent matrix computed later) from Eigen to Cartesian basis.

Equations 50 and 51 are then solved to obtain the updated values of $\boldsymbol{b}_e$. This involves the calculation of the residual and the tangent matrix as in equation 53 in the viscous branches for the local Newton loops. This corresponds to lines 5 to 13 of the algorithm. This corresponds to the line `iVar` in Fig. 2. The corresponding methods can be seen below. The calculation of residual in turn requires the calculation of the stresses in the viscous branch.

```
*(ivar+i)=((viscous+i)->dash_pot).update_intervar_Newton_principal
(F,&((viscous+i)->spring));
compute_residual_principal(material);
compute_tangent_nr_principal(material);
```

The stresses and tangents are then computed from the updated $\boldsymbol{b}_e$ (lines 14 and 17 of the algorithm, and steps `Compute stress` and `Compute tangent` in Fig. 2).

```
*(tau+i) = ((viscous+i)->dash_pot).compute_stress_tau();
*(tangent+i) = ((viscous+i)->dash_pot).rotate_mat_tan();
```

The updated values of the stress and the tangent are written into the arrays `STRESS` and `DDSDDE`, respectively. Using the updated value of $\boldsymbol{b}_e$, the viscous strains, $\boldsymbol{C}_i$ is computed. The updated values are written back into the `STATEV` array. The strain energy and the dissipation are also computed and updated (steps 15,17 and 18 of the algorithm).

```
*(STATEV+5*i+4) = *(_SSE+i) = ((viscous+i)->spring).compute_strain_energy();
*(_SCD+i) = ((viscous+i)->dash_pot).compute_dissipation();
```

The material subroutines provide the invariants I_1 and I_2 (equations 41 and 42) and the derivatives of strain energy with respect to the invariants, which are then used to compute the stresses and the tangent (as in equation 65).

To obtain the eigenvalue decomposition of $\boldsymbol{b}_e$ and other matrix operations, Eigen library [36] has been used. The expressions in [28] could have as well been used instead. It is also possible to perform the computations in the viscous

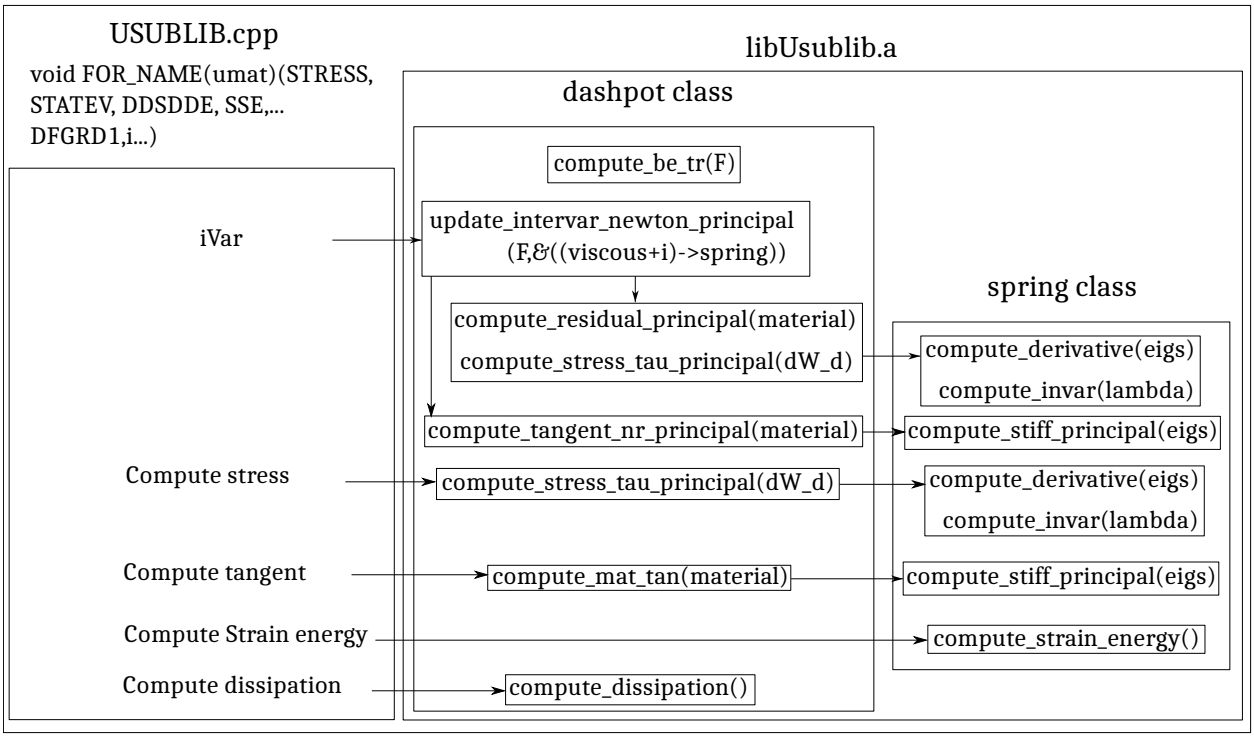

Figure 2: Figure describing a rough flow of control in the user subroutine.

branches in parallel as the computations are independent of each other. This speeds up the computations and the stresses and tangents obtained from different branches can be summed directly.

5 Comparisons with various other cases/models

In this section, the predictions of the FV model will be compared to that of the FLV model in [14]. Then, the computational times taken by the simulations performed using the plane stress version of the FV model will be compared with that of the times taken for the 3D simulations. The results of the two simulations will also be compared.

5.1 Comparison with the FLV model

The predictions of the model when the relaxation times are smaller are expected to coincide with the hyperelastic case. This will be checked in the A. The predictions of the FLV and FV models in small strains with small perturbations and large strains with small perturbations can also be seen in A. Here, the case of large strains and large perturbations will be considered as they will help with the interpretation of the results presented in the later sections.

The geometry used for this purpose is similar to what will be used to analyze the fracture experiments in the later sections. A rectangular specimen that is $40\,\mathrm{mm}$ tall and $200\,\mathrm{mm}$ long was used in the fracture experiments. To compare the predictions of the FV and the FLV models, a loading similar to that in [15] will be used. The loading is as follows (see Fig. 3):

- Holding the bottom boundary of the body stationary, the top boundary will be subjected to a vertical displacement of 2δ in $0.1\,\mathrm{sec}$.
- The stress in the specimen will then be monitored for a span of $30\,\mathrm{sec}$ while the applied displacements are held fixed.

Currently, only the top half of the specimen has been modeled taking advantage of the symmetry of the geometry and the loading. The body has been meshed with plane stress quadrilateral (CPS4) elements. An element size of $1\,\mathrm{mm}$ has been used. This results in a total of 4000 elements. The geometry and the mesh used can be seen in Fig. 3. The stress

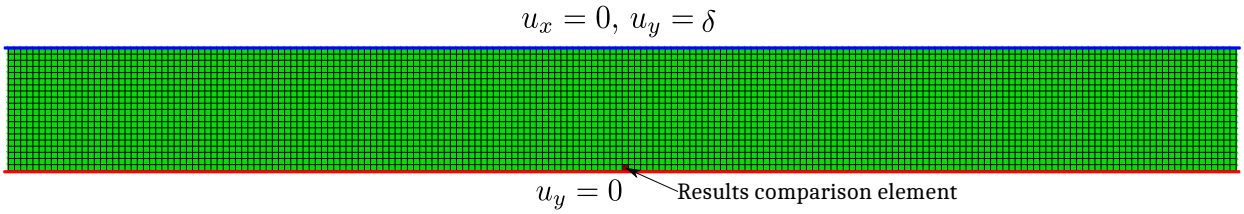

Figure 3: Geometry and the mesh used to compare the results of the FV model with the FLV model. The geometry is $20\,\mathrm{mm} \times 200\,\mathrm{mm}$ (only the top half of the test specimen). A vertical displacement of δ is applied on the top part (in blue) of the boundary, while restraining any horizontal movement. The bottom part (in red) is constrained from moving on the vertical direction, while free to move horizontally.

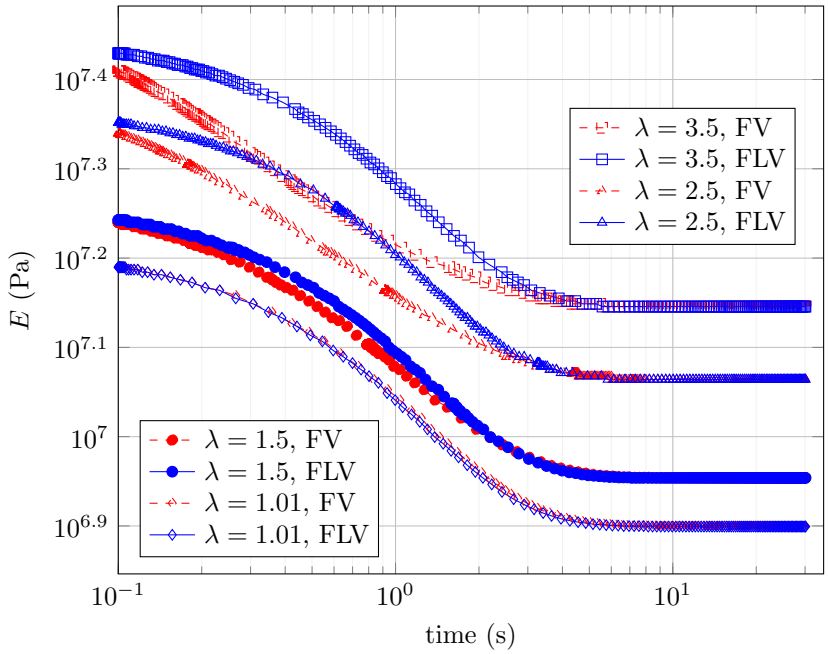

Figure 4: Evolution of modulus predicted by FLV and FV models for various stretch levels. Differences in predictions between the two models can be seen at higher stretches.

values in the element shaded in brown (which is almost at the center of the specimen) will be extracted and compared for the two models. An implementation of the FLV model is already present in Abaqus.

The hyperelastic and the viscoelastic branches of the model have been represented by the Polynomial model presented in A. The model parameters can be seen in table 6. Only one viscous branch has been used and model parameters for the viscous branch have been taken to be equal to that of the hyperelastic branch. The relaxation time has been chosen to be $1\,\mathrm{s}$.

The evolution of the $yy-$component of the Cauchy stress tensor has been monitored. The relaxation function is defined as $E(t) := \sigma(t)/\ln(1+\delta/L)$, where $L = 20\,\mathrm{mm}$. The results of the predictions for $\delta = [2\,\mathrm{mm}, 10\,\mathrm{mm}, 30\,\mathrm{mm}, 50\,\mathrm{mm}]$ from FLV and FV models can be seen in Fig. 4.

It can be seen that at small stretches (1.01), the predictions of FLV and the FV models remain very close to each other. However, as the stretch levels increase, differences between the two models increase. The FV model predicts a faster decay compared to the FLV model, with the speed of decay increasing with the applied stretch. It can be interpreted that the relaxation times in the FV model move towards smaller values with increasing strains. In the case of the FLV model, the curves can be seen to merely translate upwards at different strain levels. These predictions are in line with what has been observed in Fig. 4.3 of [15], where the analysis has been performed assuming plane strain conditions prevail.

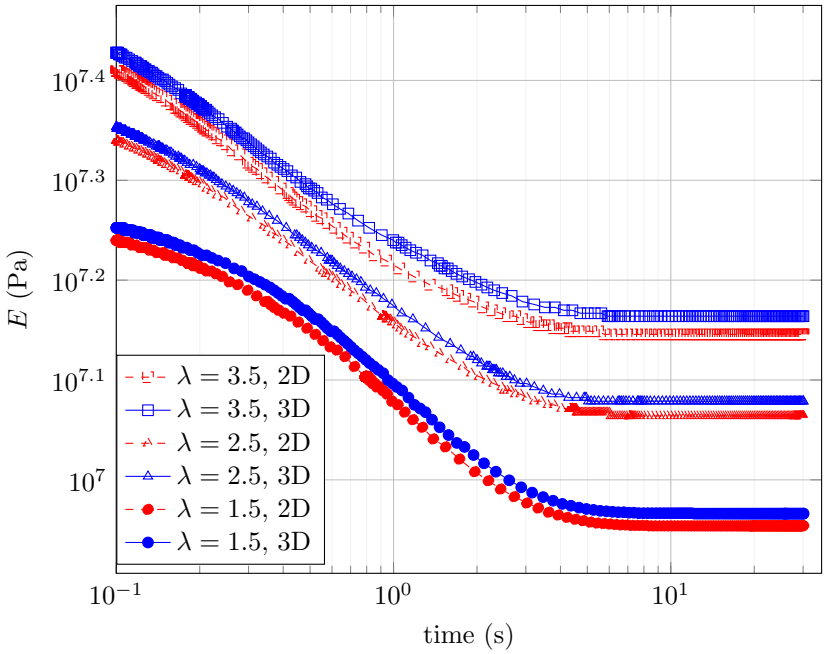

Figure 5: Evolution of modulus predicted by 2D and 3D simulations.

5.2 Comparison of the plane stress FV model with 3D simulations

The simulations from the previous section have been run this time in 3D to compare the times taken in each case and the closeness of results in both cases. For this purpose, a specimen similar to that in Fig. 3 has been considered, with the thickness taken to be $3\,\mathrm{mm}$ like in the experiments. It is then meshed by C3D8H hybrid brick elements with linear displacement and constant pressure within the element. The element size is $1\,\mathrm{mm} \times 1\,\mathrm{mm} \times 0.75\,\mathrm{mm}$ ($0.75\,\mathrm{mm}$ is along the thickness direction). This results in a total of $16\,000$ elements. The loading conditions are the same as earlier, except that the top face is constrained from moving along the thickness direction as well ($u_z = 0$).

The deviatoric part of the evolution equations for the viscous strains in the FV model of [18] can be seen to be a special case of [21]. By setting $C_2 = 0$, $m = 1$, and $C_1/(\sqrt{2}\hat{\tau}_B) = 1/(2\eta_D)$ in equations 17 and 24 of [21], the deviatoric part of equation 25 of [18] can be recovered. These parameters have been used in the Bergstorm-Boyce model of Abaqus to perform the simulations in the 3D case. In the documentation of Abaqus (Nonlinear viscoelasticity - Parallel Rheological Framework), the flow rule of the BB model can be seen to be (choosing $m = 1$, $C = 0$).

$$-\frac{1}{2}\mathcal{L}_v \boldsymbol{b}_e . \boldsymbol{b}_e^{-1} = \frac{3A}{2}\bar{\boldsymbol{\tau}}. \tag{83}$$

The parameter A in the BB model can hence be identified as $A = 1/(3\eta_D)$ (compare the above with equation 24). One viscous branch has been used like in the earlier simulations.

The simulations have been performed on an Intel(R) Core(TM) i7-8750H CPU @ 2.20GHz. The results of the simulations (the variation of E with time as in the previous section), together with the results from the 2D simulations can be seen in Fig. 5. It can be seen that the results from both simulations are quite close to each other for the cases presented. The maximum difference in the results together with the times taken for the simulations can be seen in table 2. The maximum difference in E between both cases can be seen to be 4.6%. Refining the meshes and reducing the specimen thickness might bring the results even closer. A significant speedup can be noticed between the 2D and 3D simulations. The 3D simulations can be seen to take about 20 times more time than the 2D simulations.

The case where $\lambda = 2.5$ has been run again in the 2D and 3D cases, but this time with 7 viscous branches with properties as in table 4. This increases the number of local Newton loops performed. For this case, the maximum difference in the value of E was found to be 3.2%. The 2D simulation took a CPU time of $786.67\,\mathrm{sec}$ and the 3D simulation took a CPU time of $24\,865.0\,\mathrm{sec}$. The observed speedup is thus significant.

Table 2: Maximum difference in the relaxation modulus and simulation times for the 2D and 3D simulations.

Stretch ratio	$\max_t \frac{\lvert E_{3d}(t)-E_{2d}(t)\rvert}{E_{3d}(t)}$	CPU time (sec) for 2D	CPU time (sec) for 3D
1.5	4.2%	367.56	8483.9
2.5	4.1%	526.05	9034.8
3.5	4.6%	285.62	7032.6

6 Application to viscoelastodynamic fracture

Energy is dissipated during the propagation of a crack in an elastomer membrane typically through two sources: first, as fracture energy by the creation of new fracture surfaces (also called the intrinsic fracture energy - see Section 5 of [12]) and second, through the viscoelastic effects of the bulk material. Earlier studies on crack propagation in elastomers such as in [1, 2, 5] used analytical expressions obtained by making simple assumptions on the geometry of the specimen to compute the energy consumed during the fracture processes. For instance, when a crack propagates in an infinitely long specimen (also called a pure shear configuration) under steady-state conditions (when the fields do not change for an observer moving with the crack tip), the energy release rate is computed as Wh_0, where W is the strain energy density in the material far in front of the crack and h_0 is the initial specimen height. The material is, however, assumed to be elastic and the strains in the material behind the tip are assumed to be zero.

In viscoelastic solids, the material behind the tip may not completely relax to a strain-free state, particularly when the specimen is of finite length. In such a case, the strain energy locked in the material behind the tip is to be accounted for when computing the total energy dissipated during the crack propagation. A brief discussion in this regard can be found in [37] in the case of plasticity and [11] for viscoelastic materials. In [11], an *effective tearing energy* has been defined based on the strains leftover in the material once the crack passes through.

The energy consumed by a moving crack in a viscoelastic solid has been studied analytically in [38, 39, 12] and the references therein. Using the extended correspondence principle, the stress fields in the vicinity of a crack in a viscoelastic solid are calculated in terms of the stresses in an equivalent elastic solid. The energy dissipated is thus computed. The energy dissipated was seen to be the product of the *intrinsic fracture energy* of the solid multiplied by a factor that depends on the viscoelastic properties of the body and the crack speed. The problem of crack propagation in inelastic materials has been studied using the material forces in [40]. In that reference, the energy dissipation for crack growth in an elastoplastic and a viscoelastic solid has been studied. The material in the vicinity of the crack tip was found to dissipate energy along with the energy dissipation in the material undergoing failure at the crack tip. In [41], crack propagation in an infinitely long viscoelastic strip has been studied using a cohesive zone model. The energy dissipated by the crack and the development of viscoelastic zone was studied as a function of various non-dimensional parameters. It was observed that the region where the energy is dissipated in the bulk material moved further from the tip with an increase in crack speed and was completely detached from the tip after some crack speed. The fracture energy was observed to increase with an increase in the crack speed similar to what will be presented later in the article and what has been observed in [42].

In cases where the deformation fields in the (almost) entire body are accessible (through the DIC technique, for instance), the energy dissipated through viscoelastic effects can be computed more accurately using the procedure detailed in the following. The methodology followed in this study is similar to what has been done in [13] and will be described briefly in the following. The propagation of a crack in Polyurethane elastomers has been studied in [8]. In that study, sheets of Polyurethane elastomers (in pure shear configuration) are first stretched to a target level and a crack is then introduced (see Fig. 6). The crack then propagates through the specimen at speeds that depend on the stretch level. DIC technique [43] has been used to obtain the displacement fields in the body during the propagation of the crack. The displacement fields along the region near the crack face are extracted throughout the duration of the experiment.

A FE model that represents the top half of the specimen has been considered in this study. The displacement history of the points that are along the crack path that was extracted earlier are imposed on the FE model as time-varying Dirichlet boundary conditions (see Fig. 7). This way, the crack speed is implicitly imposed on the FE model. It shall be noted that the displacements have not been extracted exactly along the crack face, but rather at some distance from it. This is

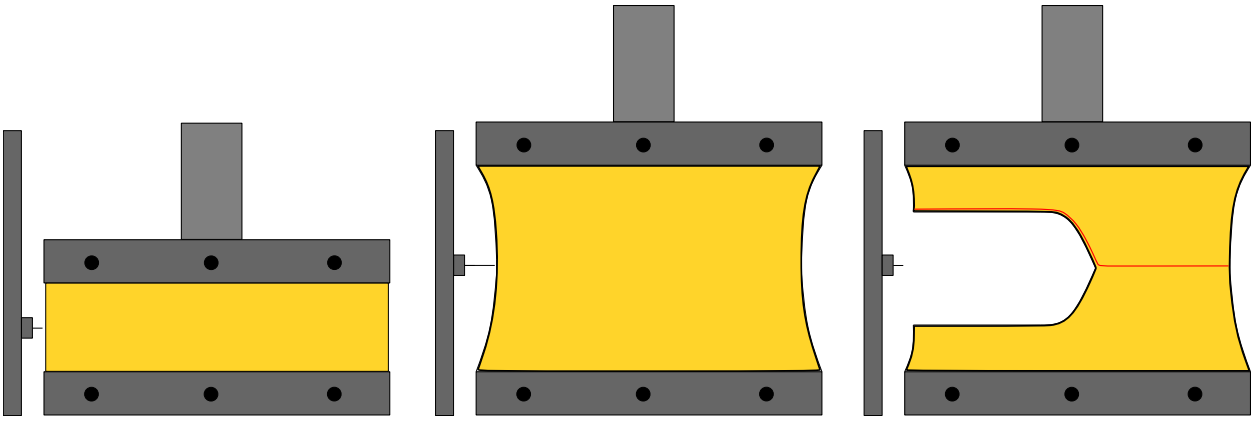

Figure 6: Experimental setup to study the fracture of Polyurethane samples. In the first figure, the specimen is held between the jaws of tensile machine. It is then stretched to the target level as in the middle figure and a small crack is then introduced using a razor blade. The crack propagates through the specimen breaking it into two parts as in the figure on the right. Displacements are extracted along the red line in the figure on the right as the crack propagated through.

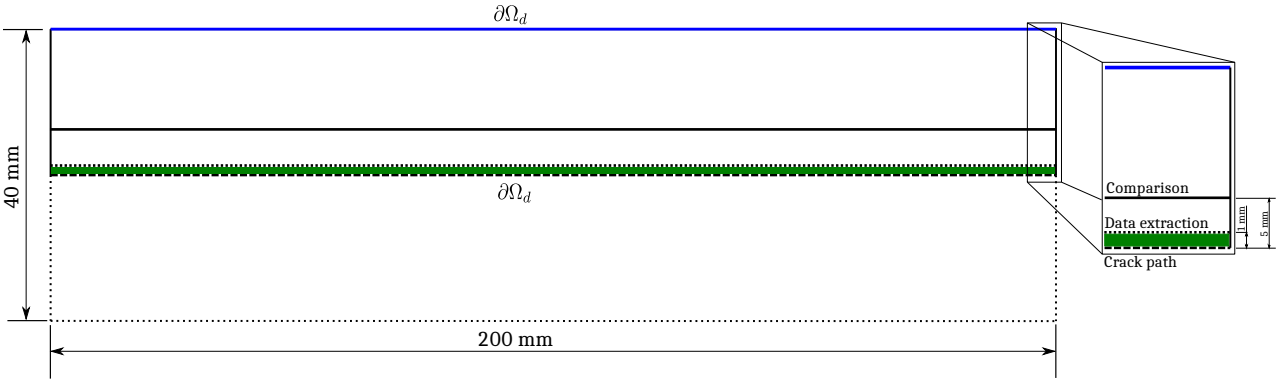

Figure 7: Geometry used in the current study. Only the top half is modeled as a consequence of symmetry. The prospective crack path in the undeformed configuration has been represented as dashed line, which is also the line of symmetry. The dotted line is about $1\,\mathrm{mm}$ away from the dashed line in the undeformed configuration and the displacement boundary conditions are applied along this line. The fields of interest will be extracted along the solid line which is about $5\,\mathrm{mm}$ away from the crack path and compared between the simulations and the experiments.

a consequence of the limitations of the DIC technique as a result of which the displacements are unavailable in the near tip region exactly along the crack faces. The images on which the DIC was performed can be found at [44].

The applied boundary conditions are:

- Constraining the bottom part of the specimen (in red in Fig. 8) from moving in the vertical direction, the top part (in blue) is moved to achieve the target stretch level. The top part is constrained from moving horizontally.
- The top part is then held fixed. The displacements extracted from the experiments as described in Figs. 6 and 7 are imposed on the nodes in the red region as Dirichlet boundary conditions.

The applied boundary conditions are similar to what the specimen will experience during the course of the experiment.

6.1 With same relaxation times and stiffness ratios as that of the FLV model

In the fracture experiments performed in [8], the cracks propagated at speeds of about $40\,\mathrm{m\,s^{-1}}$ and $56\,\mathrm{m\,s^{-1}}$ for initial stretch levels of 2.5 and 3.5, respectively. The elastic shear wave speed for Polyurethane elastomer was found to be about $40\,\mathrm{m\,s^{-1}}$. Hence, the cracks are said to propagate in the $r-$Transonic regime [13] at these stretch levels. An

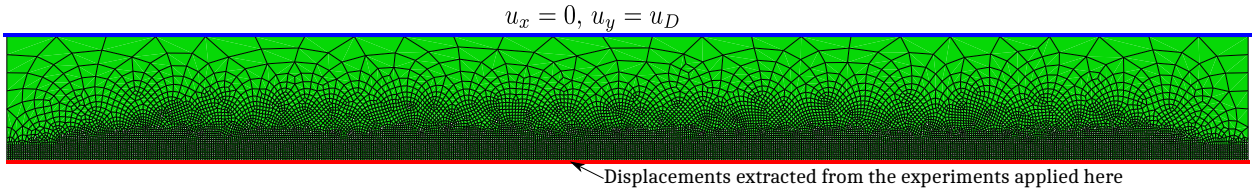

Figure 8: Mesh used for the analysis. The displacements extracted using the DIC technique have been applied on the nodes along the red line, while the nodes at the top in blue are held fixed at the target level.

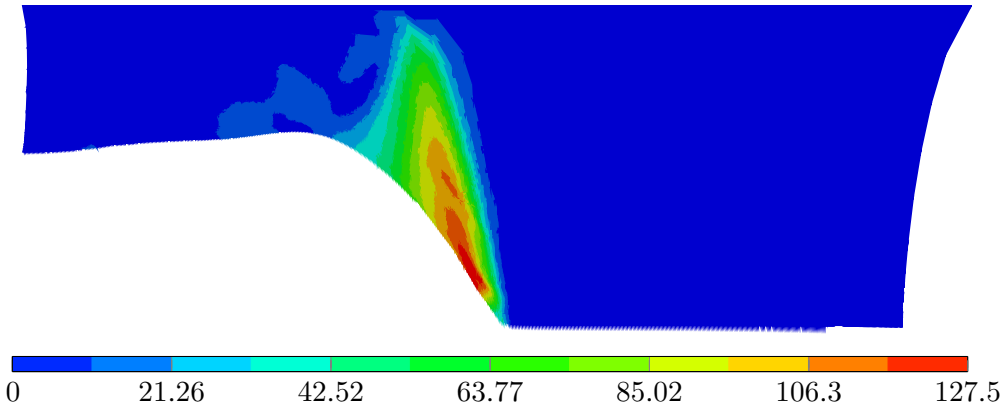

Figure 9: Particle velocity (in $\mathrm{m\,s^{-1}}$) profile for $\lambda = 3.5$, plotted on the deformed configuration.

energetic analysis will be performed for these two cases in this article. The 4-node bi-linear plane stress element (CPS4 in Abaqus) will be used for this purpose. An element size of $0.3\,\mathrm{mm}$ has been used along the crack path with the size increasing gradually to about $5\,\mathrm{mm}$ in regions far from the crack path. The mesh used for this study can be seen in Fig. 8. HHT-α method [25] has been used to integrate the momentum equations in time implicitly. The parameters of the algorithm have been chosen to be $\alpha = -5 \times 10^{-2}$, $\gamma = 0.55$, and $\beta = \gamma/2$.

The analysis

The analysis will be first performed by assigning $\gamma_0 = 1$ and choosing the same stiffness ratios (g_i) and relaxation times (τ_i) as that in the FLV model calibrated in [13] (repeated in table 3 for convenience). It shall be noted that the stiffness ratios of the FLV model in [13] are with respect to the glassy modulus and hence, they are to be scaled using the relation $(g_i)_{\text{rubbery}} = \frac{(g_i)_{\text{glassy}}}{1-\sum_{i=1}^{N}(g_i)_{\text{glassy}}}$ to obtain the stiffness ratios with respect to the rubbery modulus. Also, only 8 branches have been used in the current study (this will be justified later on). The results of this analysis are however expected to be different from what has been observed in the aforementioned article, as the predictions of both the models differ for configurations that are far from equilibrium as seen in section 5.1. For instance, the velocity fields for the case of $\lambda = 3.5$ can be seen in Fig. 9. The velocity profile observed during the experiments can be found in Fig. 2c of [13].

Table 3: Relaxation times and stiffness ratios for $\gamma_0 = 1$.

Branch	1	2	3	4	5	6	7	8
Stiffness ratio (glassy)	0.0005	0.0012	0.0011	0.0014	0.005	0.01	0.2	0.02
Stiffness ratio (rubbery)	0.0529	0.128	0.121	0.157	0.5298	1.0589	21.178	2.11
Relaxation time (s)	10^{-1}	10^{-2}	10^{-3}	10^{-4}	10^{-5}	10^{-6}	10^{-7}	10^{-8}

The velocity distribution when the crack is about at the center of the specimen has been extracted along the solid line in Fig. 7 for the current simulations and from the experiments, along with simulations using a polynomial hyperelastic

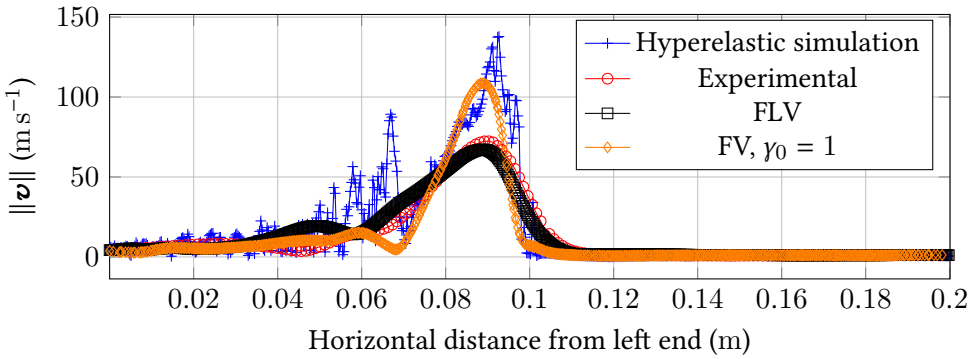

Figure 10: Particle velocity comparison at about $5\,\mathrm{mm}$ above the crack path for different models. Results for the FLV model were obtained from [13].

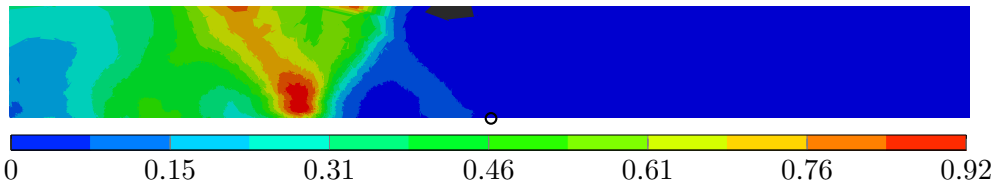

(a) The distribution of $\beta_2 = \frac{\psi_2}{\psi_\infty}$ when the crack is at about the center of the specimen.

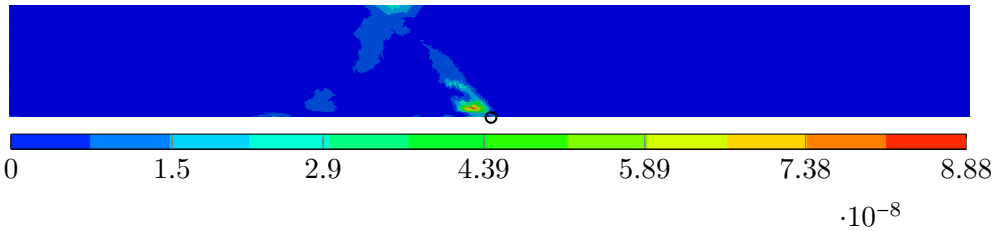

(b) The distribution of $\beta_8 = \frac{\psi_8}{\psi_\infty}$ when the crack is at about the center of the specimen.

Figure 11: β_i for the second and the eighth viscous branches. The position of the crack tip is indicated by small circles.

model from [13]. The velocity distribution for all three cases can be seen in Fig. 10. It can be seen that the predictions of the FV model are far from the experimental results and are close to the predictions of the hyperelastic model, but without exhibiting any jumps. Also, the maximum value of velocity is closer to the hyperelastic case.

As can be seen in section 5.1, the FV model shifts the relaxation times to smaller values at larger strains. Since viscoelastic effects are responsible for the absence of the shock-front-like feature in the simulations using the FLV model, it can be seen that the shift in the relaxation times in the FV model results in 'not enough' viscous effects. Hence, the results tend to be closer to the hyperelastic case.

6.1.1 Activity of viscous branches

The contribution of the i^{th} viscous branch to the stiffness of the material can be obtained by examining the ratio $\beta_i := \frac{\psi_i}{\psi_\infty}$, where ψ_i denotes the strain energy in the i^{th} viscous branch computed from the corresponding elastic strain ($\boldsymbol{b}_e^i$) and ψ_∞ is the strain energy in the hyperelastic branch computed from the overall deformation. A value of 0 for the ratio indicates that the branch is inactive, $\boldsymbol{b}_e^i = \boldsymbol{I}$. If $\boldsymbol{b}_e^i = \boldsymbol{b}$, the ratio, β_i, will equal the corresponding stiffness ratio, g_i, of the branch. β_i can take values greater than g_i in cases where the hyperelastic branch is relatively unloaded while the viscous branch is still active. The ratio for the 2^{nd} and the 8^{th} viscous branches with relaxation times of $10^{-2}\,\mathrm{s}$ and $10^{-8}\,\mathrm{s}$, respectively, plotted on the undeformed configuration can be seen in Fig. 11.

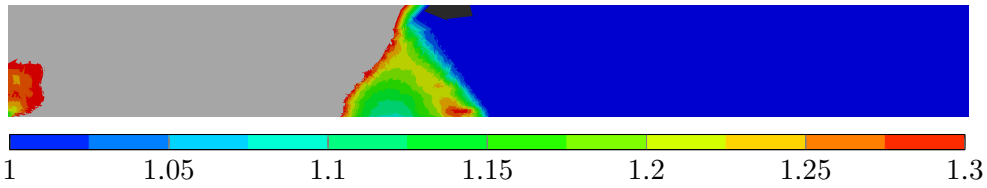

Figure 12: Distribution of β when $\gamma_0 = 1$.

It can be seen that the maximum value of β_8 is about 9×10^{-8}, which is negligible when compared to the corresponding stiffness ratio, $g_8 = 2.11$, while for the second viscous branch, the maximum value is about 0.92. This indicates that the second viscous branch is 'more active' than the eighth and that the activity of the viscous branches decreases with a decrease in the corresponding relaxation times. It can hence be concluded that the contribution of viscous branches with smaller relaxation times will be even smaller. Hence, including them in the analysis will not result in an improvement in the results, despite the additional computational costs involved.

6.1.2 Overall viscous indicator

Also, the departure of the body from its long term elastic behavior can be studied by examining the overall viscous indicator parameter, β, defined as

$$\beta := \frac{\psi_\infty + \sum_{i=1}^{N} \psi_i}{\psi_\infty} = 1 + \sum_{i=1}^{N} \frac{\psi_i}{\psi_\infty} = 1 + \sum_{i=1}^{N} \beta_i. \tag{84}$$

A value of 1 for β indicates a purely long-term elastic behavior, while any departure from 1 indicates the presence of viscoelastic effects. The distribution of β when the crack is at about the center of the specimen can be seen in Fig. 12.

It can be seen that corresponding to the velocity profile, the value of viscous indicator is seen to raise above 1 behind a sharp front-like feature. The scale has been truncated at 1.3 to bring out the features of the distribution.

6.2 With different stiffness ratio and relaxation times from the FLV model

To bring the predictions of the model closer to the experiments, it is necessary to change either the relaxation times and/or the stiffness ratios of the model. This has been achieved by first changing the value of γ_0 to $\frac{1}{60}$. It shall be noted that doing this is equivalent to multiplying the relaxation times of all the viscous branches by a factor of 60. Also, by examining the β_is defined in the previous section, it was found that including the eighth viscous branch in the analysis does not affect the results despite the additional computational cost and hence has been removed. The stiffness ratios of the sixth and seventh branches were also adjusted to bring the observed velocity results closer to the experiments. The new parameters can be seen in the table 4.

Table 4: Relaxation times and stiffness ratios for $\gamma_0 = \frac{1}{60}$.

Branch	1	2	3	4	5	6	7
Stiffness ratio (rubbery)	0.0529	0.128	0.121	0.157	0.5298	1.1589	1.9
Relaxation time (s)	10^{-1}	10^{-2}	10^{-3}	10^{-4}	10^{-5}	10^{-6}	10^{-7}

The results of the velocity profile plotted on the deformed configuration, can be seen in Fig. 13. The velocity field, in this case, is closer to the experiments than it was when $\gamma_0 = 1$. The velocity variation at about $5\,\mathrm{mm}$ from the crack path can be seen in Fig. 14. The velocity distribution can be seen closer to the experiments.

The distribution of β for this case can be seen in Fig. 15. It can be seen that the values of β in this case are higher than what has been observed in Fig. 12 when $\gamma_0 = 1$.

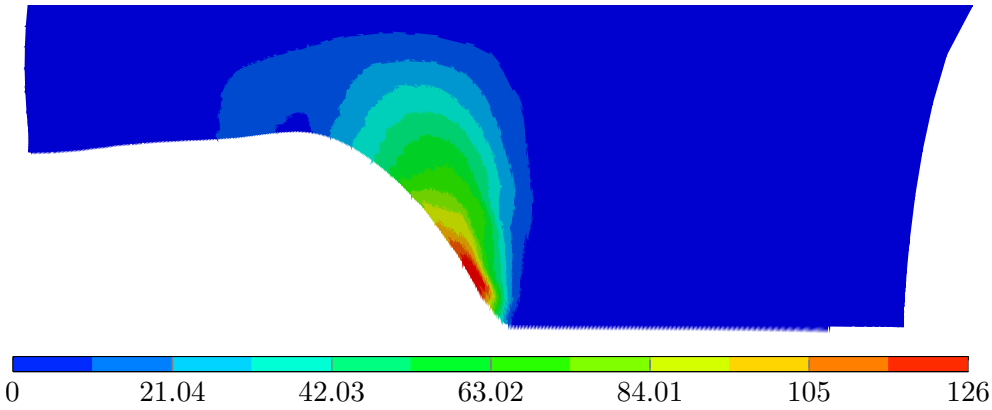

Figure 13: Particle velocity (in $\mathrm{m\,s^{-1}}$) profile for $\lambda = 3.5$, plotted on the deformed configuration.

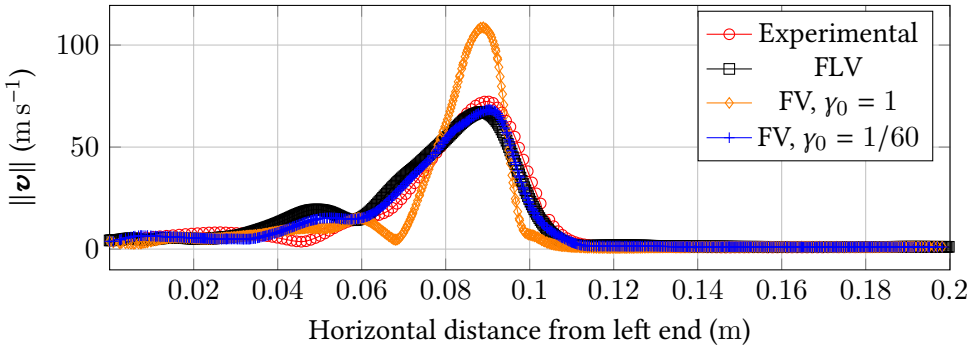

Figure 14: Particle velocity comparison at about $5\,\mathrm{mm}$ above the crack path for different models. Results for the FLV model obtained from [13].

6.3 Energy budget

Since the particle velocity predictions from the model are closer to the experiments, the energy evolution in the body during the propagation of a crack in the material can be examined. In the experiments performed on the fracture of elastomers such as in [2, 8, 45, 9], the body is first stretched to a target level. The external work done on the system during the stretching process is stored as the internal strain energy (SE) in the body. When a crack is then imparted in the body, it propagates through the body thereby releasing the stored strain energy, consuming a part of it during the fracture process. If the body is viscoelastic, a part of the strain energy is also consumed as viscoelastic dissipation (D) and some portion of the SE is also converted into kinetic energy (KE).

The evolution of strain energy (SE), kinetic energy (KE), and viscoelastic dissipation (D) energy of the body with time can be monitored as the crack passes through it and their rates can be computed. The release rates of the corresponding energy quantities can then be calculated using their rates of evolution. Denoting the work done by the external forces when the crack passes through the body as W, the strain energy (SER), kinetic energy (KER), dissipation (DR), and

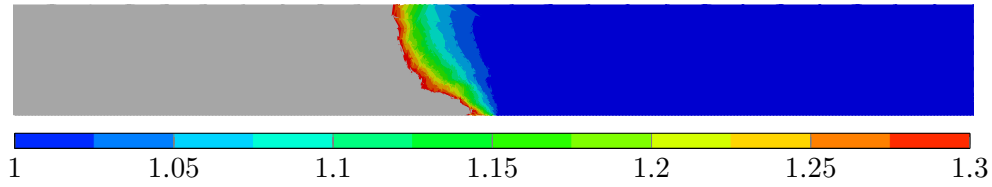

Figure 15: Distribution of β when $\gamma_0 = \frac{1}{60}$.

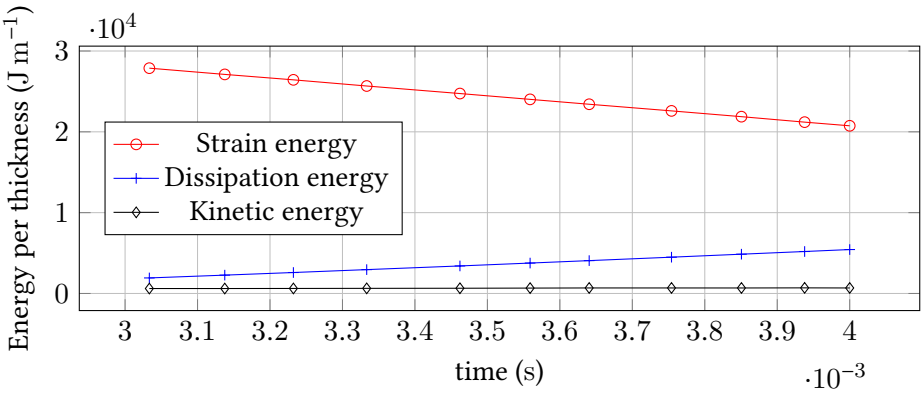

Figure 16: Evolution of different energies with time for $\lambda = 3.5$. Experiments performed in [8].

the external work (WR) release rates can be defined as

$$SER = -\frac{1}{w_0}\frac{\mathrm{d}SE}{\mathrm{d}t}, \tag{85}$$

$$KER = \frac{1}{w_0}\frac{\mathrm{d}KE}{\mathrm{d}t}, \tag{86}$$

$$DR = \frac{1}{w_0}\frac{\mathrm{d}D}{\mathrm{d}t}, \tag{87}$$

$$WR = \frac{1}{w_0}\frac{\mathrm{d}W}{\mathrm{d}t}. \tag{88}$$

In the above, w_0 is the crack speed. The power of external forces can be computed as

$$\frac{\mathrm{d}W}{\mathrm{d}t} = \frac{\mathrm{d}SE}{\mathrm{d}t} + \frac{\mathrm{d}KE}{\mathrm{d}t} + \frac{\mathrm{d}D}{\mathrm{d}t}. \tag{89}$$

As the crack passes through the body, its top surface is stationary (held using the grips in the tensile machine as in [8]). Hence, the external forces acting on this part of the body do no work during this time. The lateral surfaces of the body are traction free and hence do not contribute to the external work as well. Along the bottom surface, however, as the crack propagates through, the cohesive tractions acting near the crack tip, together with non-zero particle speeds, extract work from the body. Also, in the current scenario, the portion of the body that is about $1\,\mathrm{mm}$ from the crack path is not included in the analysis (the area shaded in green in Fig. 7). Hence, the work done by the external forces in the current case also includes the viscoelastic energy dissipation in the material that is not included, along with the work done by the cohesive forces.

The evolution of energies can be observed in Fig. 16 for the case when $\lambda = 3.5$. A similar procedure can be performed for other experiments (when $\lambda = 2.5$, for instance) as well. Once done, the corresponding slopes can be computed, using which the release rates can be obtained. The results thus obtained can be seen in the table 5. It shall be noted that a factor of 2 has been added to the definitions of energy release rate since only the top half of the model has been considered for the current study. P_{ext} has been used in place of dW/dt. Also can be seen are the quantities ψh_0 and $[\![\psi]\!]h_0$, which are typically used to compute the energy release rates from experiments [1]. h_0 is the initial specimen height and ψ denotes the strain energy density in the material in front of and far from the tip when the tip is about at the center of the specimen (since the body is finite in the current scenario, far in front of the tip refers to about $50\,\mathrm{mm}$ in front of the current tip location). $[\![\psi]\!]$ denotes the jump in strain energy density, which is the difference in the strain energy densities in the material between far in front of and behind the tip (behind the tip refers to about $50\,\mathrm{mm}$ behind the current tip location).

The results in table 5 warrant some observations. As expected, the strain energy decreases as the crack passes through (as can be seen by the negative sign in front of the expression for the release rate). The viscoelastic dissipation is positive, and the kinetic energy rate is an order or two smaller than the strain energy release rate. The majority of the strain energy is consumed as viscous dissipation (in the bulk and the material not included in the analysis) and the fracture processes. Between the two cases presented, it can be observed that the viscoelastic energy dissipation

Table 5: Energy release rates for the experiments in $\mathrm{kJ/m^2}$.

λ	$-\frac{2}{w_0}\frac{\mathrm{d}SE}{\mathrm{d}t}$	$\frac{2}{w_0}\frac{\mathrm{d}D}{\mathrm{d}t}$	$\frac{2}{w_0}\frac{\mathrm{d}KE}{\mathrm{d}t}$	$-\frac{2}{w_0}P_{ext}$	ψh_0	$[\![\psi]\!]h_0$
2.5	130	49	8.5	76	166	120
3.5	260	129	2.0	127	348	268

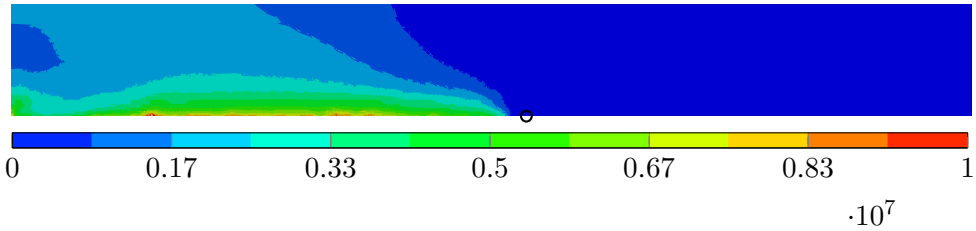

Figure 17: Viscoelastic energy dissipation density (in $\mathrm{J/m^3}$) for $\lambda = 3.5$. The approximate position of crack tip is indicated by a small black circle.

(quantified by the term $\frac{2}{w_0}dD/dt$ in the table 5) increases with an increase in crack speed. The external work can be seen to increase as well. However, it shall be noted that the external work ($-\frac{2}{w_0}P_{ext}$) in this case also includes the dissipation in the region shaded in green in Fig. 7. A more accurate decomposition of the energy consumption requires the data to be extracted much closer to the crack path, which was not possible since the data in the pixels close to the crack faces are lost when using the DIC technique.

In [13], it was observed that the strains in the material behind the tip do not go to zero after the crack tip passes through. This is a consequence of the presence of relaxation times larger than the experimental duration (about $1\,\mathrm{ms}$). This results in some strain energy being locked in the material behind the tip even after the crack tip passed through. Hence, it can be seen that the strain energy release rate equals the quantity $[\![\psi]\!]h_0$ rather than ψh_0. This stresses the importance of including the viscoelastic effects in the analysis of the problem. It shall be noted that a somewhat similar analysis has been performed experimentally in [11].

Also, the region in the body where the energy is dissipated can be seen in Figs. 17 and 18 for the case of $\lambda = 3.5$ when the crack is at about the center of the body. The quantity that has been plotted in Fig. 17 is $\int_0^t \mathcal{D}\,\mathrm{d}t$ (energy dissipated) and the quantity plotted in Fig. 18 is $\mathcal{D}$ (energy dissipation rate), where the expression for $\mathcal{D}$ can be seen in equation 82. It can be seen that there is a significant viscoelastic energy dissipation rate in the material in the vicinity of the crack tip. The region of dissipation observed in Fig. 18 can be seen to be similar to that in [41] (Figs. 8,11, and 13 of the reference) - in the vicinity of the tip. The dissipation rate takes a maximum value near the tip, while gradually reducing when moving further away. Also, the dissipated energy is confined to the regions behind the tip, extending to the boundary while there is no dissipation in the region ahead of the tip. This is consistent with the observations made earlier that the material ahead of the tip behaves in an elastic manner.

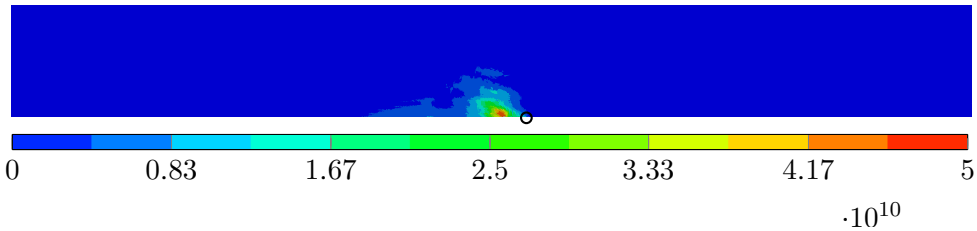

Figure 18: Viscoelastic energy dissipation density rate (in $\mathrm{J/\,sec\,/m^3}$) for $\lambda = 3.5$. The approximate position of crack tip is indicated by a small black circle.

7 Conclusions

A plane stress version of the FV model has been presented in this article together with its implementation into the UMAT subroutine of Abaqus [24]. The plane stress version of the model significantly reduces the computational costs as a pure displacement (u) based 2D FE simulations can be performed as opposed to using mixed (such as displacement/pressure) methods (in 3D) as in [20]. Also, enforcing $F_{33} = 1/\det \boldsymbol{F}^{2d}$ in elastic and viscous branches reduces the size of the system being solved while determining the eigenvalues of $\boldsymbol{b}_e^{tr}$ and during the Newton iterations while solving equations 28 from 3×3 to 2×2. The numerical integration procedure is similar to that in the 3D case. The only difference is that the expressions for stresses and the tangents are obtained after enforcing the incompressibility ($F_{33} = 1/\det \boldsymbol{F}^{2d}$) and plane stress ($\tau_{33} = 0$) conditions. The HHT-$\alpha$ method [25] has been used in the current study to implicitly integrate the momentum equations in time as the stable time step with an explicit scheme was found to be small.

The plane stress version of the FV model has been used to perform an energetic analysis of the viscoelastodynamic fracture of Polyurethane elastomers tested in [8]. The region in the body where the viscoelastic effects are active could be determined as a consequence of the availability of strain energy density functional. Viscoelastic effects can be seen to become active in the region behind the tip - once the crack has passed through the material and the material begins to move upward toward the boundaries. Comparing the results from the analyses with different relaxation times, it can be seen that the viscoelastic effects prevent the formation of the shock-front-like feature in the Transonic regime. The velocity predictions of the FV model have been observed to be closer to the experiments. The energy dissipated in the body as a consequence of viscoelastic dissipation has been computed. It was observed that a significant portion of the energy consumed is dissipated through viscoelastic effects. It shall be noted that the presented methodology allows for determining the energy dissipated in the bulk and the energy consumed by the fracture processes for cases where the data is available up to the crack faces.

It shall be noted that instead of extracting the displacement fields near the crack faces and imposing them on the FE model, the displacement fields in the entire body (obtained by using the DIC technique) can be used directly to evaluate energy evolution. The strain fields and their evolution in time can be evaluated from the displacement fields and the strain energy and the dissipation can be evaluated from them. This procedure can also be used to calibrate the constitutive model by minimizing the residuals on the equilibrium equations using the stresses computed from strains using the constitutive model [46].

References

[1] H. W. Greensmith and A. G. Thomas. Rupture of Rubber. III. Determination of Tear Properties. *Rubber Chemistry and Technology*, 29(2):372–381, 1956.

[2] Alan Gent and P. Marteny. Crack velocities in natural rubber. *Journal of Materials Science*, 17(10):2955–2960, oct 1982.

[3] Alan Gent. Adhesion and Strength of Viscoelastic Solids. Is There a Relationship between Adhesion and Bulk Properties? †. *Langmuir*, 12(19):4492–4496, 1996.

[4] Paul J. Petersan, Robert D. Deegan, M. Marder, and Harry L. Swinney. Cracks in rubber under tension exceed the shear wave speed. *Physical Review Letters*, 93(1):015504–1, 2004.

[5] A. Stevenson and A. G. Thomas. On the bursting of a balloon. *Journal of Physics D: Applied Physics*, 12(12):2101–2109, 1979.

[6] L.B. Freund. *Dynamic fracture mechanics*. Cambridge University Press, Cambridge, 1990.

[7] C. H. Chen, H. P. Zhang, J. Niemczura, K. Ravi-Chandar, and M. Marder. Scaling of crack propagation in rubber sheets. *Epl*, 96(3), 2011.

[8] Thomas Corre, Michel Coret, Erwan Verron, B. Leblé, and F. Le Lay. Experimental full field analysis for dynamic fracture of elastomer membranes. *International Journal of Fracture*, 224(1):83–100, 2020.

[9] Thanh Tam Mai, Kenichiro Okuno, Katsuhiko Tsunoda, and Kenji Urayama. Crack-Tip Strain Field in Supershear Crack of Elastomers. *ACS Macro Letters*, 9(5):762–768, 2020.

[10] A. Kadir and A. G. Thomas. Tear behavior of rubbers over a wide range of rates, 1981.

[11] A. Kadir and A. G. Thomas. Tearing of Unvulcanized Natural Rubber. *Journal of polymer science. Part A-2, Polymer physics*, 22(9):1623–1634, 1984.

[12] W.G. Knauss. A review of fracture in viscoelastic materials. *International Journal of Fracture*, 196(1-2):99–146, nov 2015.

[13] Vasudevan Kamasamudram, Michel Coret, and Nicolas Moës. The role played by viscoelasticity in the bulk material during the propagation of a dynamic crack in elastomers. *International Journal of Fracture*, 231(1):43–58, 2021.

[14] J. C. Simo. On a fully three-dimensional finite-strain viscoelastic damage model: Formulation and computational aspects. *Computer Methods in Applied Mechanics and Engineering*, 60(2):153–173, 1987.

[15] S Govindjee and S Reese. A presentation and comparison of two large deformation viscoelasticity models. *Journal of Engineering Materials and Technology, Transactions of the ASME*, 119(3):251–255, 1997.

[16] Bernard Coleman and Walter Noll. Foundations of Linear Viscoelasticity. *Rev. Mod. Phys.*, 33(2):239–249, 1961.

[17] A. Lion. A physically based method to represent the thermo-mechanical behaviour of elastomers. *Acta Mechanica*, 123(1-4):1–25, 1997.

[18] S Reese and S Govindjee. A theory of finite viscoelasticity and numerical aspects. *International Journal of Solids and Structures*, 35(26-27):3455–3482, 1998.

[19] W. G. Knauss and I. Emri. Volume change and the nonlinearly thermo-viscoelastic constitution of polymers. *Polymer Engineering & Science*, 27(1):86–100, 1987.

[20] Hüsnü Dal and Michael Kaliske. Bergström-Boyce model for nonlinear finite rubber viscoelasticity: Theoretical aspects and algorithmic treatment for the FE method. *Computational Mechanics*, 44(6):809–823, 2009.

[21] J Bergström and M Boyce. Constitutive modeling of the large strain time-dependent behavior of elastomers. *Journal of the Mechanics and Physics of Solids*, 46(5):931–954, 1998.

[22] Pedro Areias and Karel Matouš. Finite element formulation for modeling nonlinear viscoelastic elastomers. *Computer Methods in Applied Mechanics and Engineering*, 197(51-52):4702–4717, 2008.

[23] Marcos Latorre and Francisco Javier Montáns. Anisotropic finite strain viscoelasticity based on the Sidoroff multiplicative decomposition and logarithmic strains. *Computational Mechanics*, 56(3):503–531, 2015.

[24] Dassault. ABAQUS/Standard User's Manual, Version 6.14, 2014.

[25] Hans M Hilber, Thomas J R Hughes, and Robert L Taylor. Improved Numerical Dissipation For Time Integration Algorithms in Structural Dynamics. *Earthquake Engineering and Structural Dynamics*, 5(June 1976):283–292, 1977.

[26] Bernard Coleman and Morton E Gurtin. Thermodynamics with internal state variables. *The Journal of Chemical Physics*, 47(2):597–613, 1967.

[27] François Sidoroff. Un modèle viscoélastique non linéaire avec configuration intermédiaire. 1974.

[28] J. C. Simó. Algorithms for static and dynamic multiplicative plasticity that preserve the classical return mapping schemes of the infinitesimal theory. *Computer Methods in Applied Mechanics and Engineering*, 99:61–112, 1992.

[29] Gustavo Weber and Lallit Anand. Finite deformation constitutive equations and a time integration procedure for isotropic, hyperelastic-viscoplastic solids. *Computer Methods in Applied Mechanics and Engineering*, 79(2):173–202, 1990.

[30] Raymond W Ogden. *Non-linear elastic deformations*. Courier Corporation, 1997.

[31] Javier Bonet. Large strain viscoelastic constitutive models. *International Journal of Solids and Structures*, 38(17):2953–2968, 2001.

[32] S Reese and P Wriggers. A finite element method for stability problems in finite elasticity. *International journal for numerical methods in engineering*, 38(7):1171–1200, 1995.

[33] Nhung Nguyen and Anthony M. Waas. Nonlinear, finite deformation, finite element analysis. *Zeitschrift fur Angewandte Mathematik und Physik*, 67(3):1–24, 2016.

[34] J. C. Simo. Numerical analysis and simulation of plasticity. In *Numerical Methods for Solids (Part 3) Numerical Methods for Fluids (Part 1)*, volume 6, pages 183–499. Elsevier, 1998.

[35] Vasudevan Kamasamudram. UMAT for a Finite Viscoelastic model.

[36] Gael Guennebaud and Benoit Jacob. Eigen v3, 2010.

[37] L.B. Freund and J.W. Hutchinson. High strain-rate crack growth in rate-dependent plastic solids. *Journal of the Mechanics and Physics of Solids*, 33(2):169–191, jan 1985.

[38] W.G. Knauss and H.K. Mueller. Crack propagation in a linearly viscoelastic strip. *Journal of Applied Mechanics*, 38:483–488, 1971.

[39] R. A. Schapery. A theory of crack initiation and growth in viscoelastic media - I. Theoretical development. *International Journal of Fracture*, 11(1):141–159, feb 1975.

[40] T.D. Nguyen, S. Govindjee, P.A. Klein, and H. Gao. A material force method for inelastic fracture mechanics. *Journal of the Mechanics and Physics of Solids*, 53(1):91–121, jan 2005.

[41] T. D. Nguyen and S. Govindjee. Numerical study of geometric constraint and cohesive parameters in steady-state viscoelastic crack growth. *International Journal of Fracture*, 141(1-2):255–268, 2006.

[42] Vasudevan Kamasamudram. *Investigation of dynamic fracture of elastomers : On the role played by viscoelasticity*. Theses, École centrale de Nantes, December 2021.

[43] Michael A Sutton, Jean Jose Orteu, and Hubert Schreier. *Image correlation for shape, motion and deformation measurements: basic concepts, theory and applications*. Springer Science & Business Media, 2009.

[44] Michel Coret and Thomas Corre. Investigation of Dynamic Fracture of Elastomers - I., 2017.

[45] G. J. Lake, C. C. Lawrence, and a. G. Thomas. High-Speed Fracture of Elastomers: Part I. *Rubber Chemistry and Technology*, 73(5):801–817, 2000.

[46] Michel Grédiac. Principe des travaux virtuels et identification. *Comptes rendus de l'Académie des sciences. Série 2, Mécanique, Physique, Chimie, Sciences de l'univers, Sciences de la Terre*, 309(1):1–5, 1989.

[47] Gerhard A. Holzapfel. Nonlinear Solid Mechanics_ A Continuum Approach for Engineering. 2000.

[48] J Lubliner. A model of rubber viscoelasticity. *Mechanics Research Communications*, 12(2):93—-99, 1985.

A Comparison with hyperelastic and the FLV models

A.1 Model predictions for Hyperelastic case

The correctness of the implementation of the material model in the `UMAT` subroutine will be checked first starting with the hyperelastic part. The polynomial strain energy functional will be used. The results of the predictions from `UMAT` will be compared with that from the internal implementation of Abaqus to check the sanity of the implementation.

The strain energy functional for polynomial model can be seen to be [47]

$$\psi = \sum_{i,j=1}^{i+j=N} C_{ij}(I_1 - 3)^i (I_2 - 3)^j, \tag{90}$$

where C_{ij}s are the model parameters, I_1 and I_2 are the two invariants of $\bar{\boldsymbol{C}} = J^{-1/3}\boldsymbol{C}$. The computation of stresses and tangent requires the computation of $\partial\psi/\partial I_i$ and $\partial^2\psi/\partial I_i \partial I_j$, $i, j = 1, 2$ (equations 43, 44, 65). For the polynomial model with N=3, these quantities can be seen to be

$$\frac{\partial\psi}{\partial I_1} = C_{10} + 2C_{20}(I_1 - 3) + C_{11}(I_2 - 3) + 3C_{30}(I_1 - 3)^2 + 2C_{21}(I_1 - 3)(I_2 - 3) + C_{12}(I_2 - 3)^2, \tag{91}$$

$$\frac{\partial\psi}{\partial I_2} = C_{01} + 2C_{02}(I_2 - 3) + C_{11}(I_1 - 3) + 3C_{03}(I_2 - 3)^2 + 2C_{12}(I_1 - 3)(I2 - 3) + C_{21}(I_1 - 3)^2, \tag{92}$$

$$\frac{\partial^2\psi}{\partial I_1 \partial I_1} = 2C_{20} + 6C_{30}(I_1 - 3) + 2C_{21}(I_2 - 3), \tag{93}$$

$$\frac{\partial^2\psi}{\partial I_1 \partial I_2} = C_{11} + 2C_{21}(I_1 - 3) + 2C_{12}(I_2 - 3), \tag{94}$$

$$\frac{\partial^2\psi}{\partial I_2 \partial I_2} = 2C_{02} + 6C_{03}(I_2 - 3) + 2C_{12}(I_1 - 3). \tag{95}$$

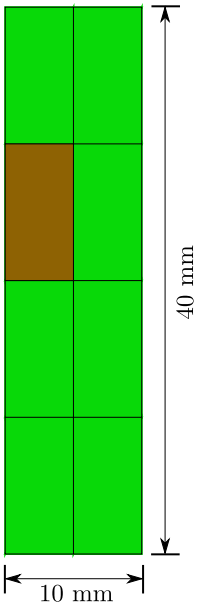

Figure 19: Geometry and mesh to test the implementation of `UMAT`.

Since ψ is smooth in I_1 and I_2, $\partial^2\psi/\partial I_1\partial I_2 = \partial^2\psi/\partial I_2\partial I_1$.

The model has been calibrated in [13] and the parameters C_{ij}s can be seen in the table 6. The rest of the parameters from table 6 are taken to be 0.

Table 6: Model Co-efficients

Parameter	C_{10}	C_{20}	C_{30}	C_{21}
Value (Pa)	1.044E6	-0.02273E6	336.0	124.0

Geometry and mesh

A rectangular-shaped body has been taken to compare the predictions of UMAT with the implementation in Abaqus. The geometry along with the mesh can be seen in Fig. 19. The top end of the sample is first subjected to displacement $u_x = 0\,\mathrm{mm},$ and $u_y = 50\,\mathrm{mm}$, while the bottom end is held fixed. The top edge is then moved horizontally by $40\,\mathrm{mm}$ so that the final displacement of the top edge is $u_x = 40\,\mathrm{mm},$ and $u_y = 50\,\mathrm{mm}$. This loading was chosen as it results in a combination of tension and shear.

Results

In the simulations performed with UMAT subroutine, the first step using 21 incremenets and the second step using 254 increments. The internal implementation of Abaqus takes 21 increments for the first step and 338 increments for the second. The $11, 12, 22$ components of Cauchy stress, $\boldsymbol{\sigma}$, predicted by the UMAT and the internal Abaqus implementation can be seen in Figs. 20, 21 and 22, respectively. From the three figures, it can be seen that the stress distributions are identical. The maximum and minimum values of $\sigma_{11}, \sigma_{12}, \sigma_{22}$ for both the cases were observed to be identical as well.

A.2 Comparison with finite linear viscoelasticity

The predictions of the model presented above will be compared with that of FLV model of [14] for some simple cases. In this and the following sections, the deviations from equilibrium are indicated by the strain levels in the viscous

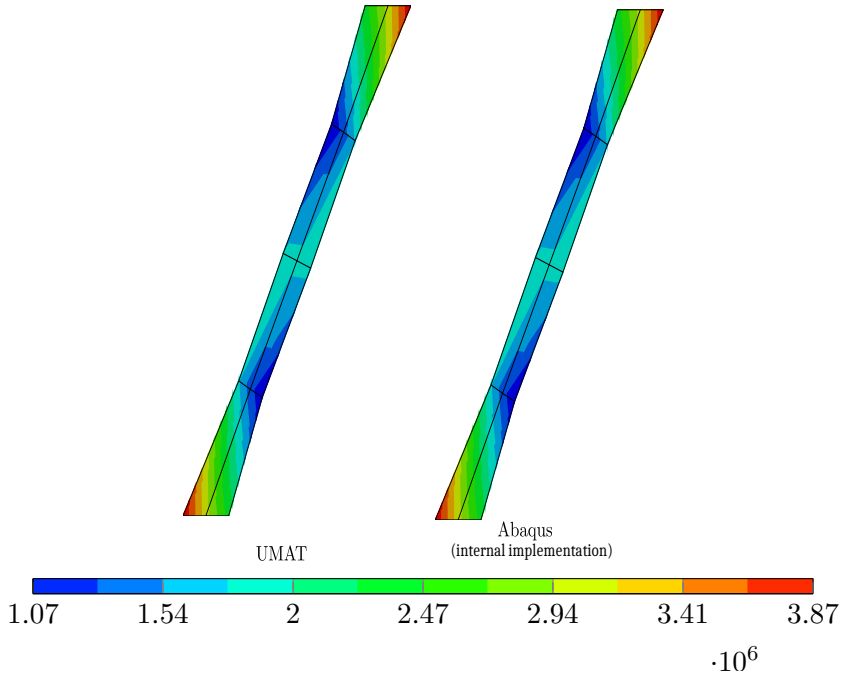

Figure 20: σ_{11} (in Pa) predicted by `UMAT` and the polynomial model from Abaqus.

branches. For instance, the case where the strains in the elastic branch are large and the strains in the viscous branches are small is indicated as *large strains and small perturbations*, while the case where the strains are large in both the elastic and the viscous branches is indicated as *large strains and large perturbations*.

The PK2 stresses in the model of [14] can be seen to be

$$\boldsymbol{S} = -Jp\boldsymbol{C}^{-1} + J^{-2/3}\mathrm{DEV}_t\left\{\boldsymbol{H}\right\}, \quad \text{where} \tag{96}$$

$$\boldsymbol{H} \coloneqq \int_0^t g(t-s)\frac{\partial}{\partial s}\left[\mathrm{DEV}_s\left\{2\frac{\partial \psi^0}{\partial \bar{\boldsymbol{C}}}(s)\right\}\right]\mathrm{d}s, \tag{97}$$

$$\mathrm{DEV}_\alpha\left\{\bullet\right\} \coloneqq \bullet - \frac{1}{3}[\bullet : \boldsymbol{C}_\alpha]\boldsymbol{C}_\alpha^{-1}, \tag{98}$$

$$g(s) = g_\infty + \sum_{i=1}^{N} g_i \exp(-s/\tau_i). \tag{99}$$

The plane stress expression for this case can be developed by finding the value of p imposing the constraint $S_{33} = 0$. The final expression can be seen to be

$$\boldsymbol{S}_{2d} = \int_{-\infty}^{t} g(t-s)\frac{\partial}{\partial s}\left[\mathrm{DEV}_s^{2D}\left\{\hat{\boldsymbol{S}}^s\right\}\right] + \frac{C_{33}^t}{3}(\boldsymbol{C}_{2d}^t)^{-1}\int_{-\infty}^{t} g(t-s)\frac{\partial}{\partial s}\left[\mathrm{tr}(\hat{\boldsymbol{S}}^s\boldsymbol{C}_{2d}^s)(C_{33}^s)^{-1}\right]. \tag{100}$$

In the above, the superscript s ot t indicates the time at which the quantity is computed and $\hat{\boldsymbol{S}} = 2\dfrac{\partial \psi}{\partial \boldsymbol{C}_{2d}}$. $\mathrm{DEV}_s^{2D}\left\{\hat{\boldsymbol{S}}^s\right\} = \hat{\boldsymbol{S}}^s - \frac{1}{3}\,\mathrm{tr}(\hat{\boldsymbol{S}}^s\boldsymbol{C}_{2d}^s)(\boldsymbol{C}_{2d}^s)^{-1}$. All this has already been implemented into Abaqus internally.

A.3 Small strains and small perturbations

Under small strain conditions, the deformation gradient can be approximated by $\boldsymbol{F} \approx \boldsymbol{I} + \boldsymbol{\epsilon}$ and hence, $\boldsymbol{C} \approx \boldsymbol{I} + 2\boldsymbol{\epsilon}$. The principal stretches can be approximated as $\lambda_1^2 \approx 1 + 2\epsilon_1$ and $\lambda_2^2 \approx 1 + 2\epsilon_2$, where the ϵ_is are the eigen values of $\boldsymbol{\epsilon}$, the small strain tensor. The small perturbation assumption allows similar approximations for the viscous branches

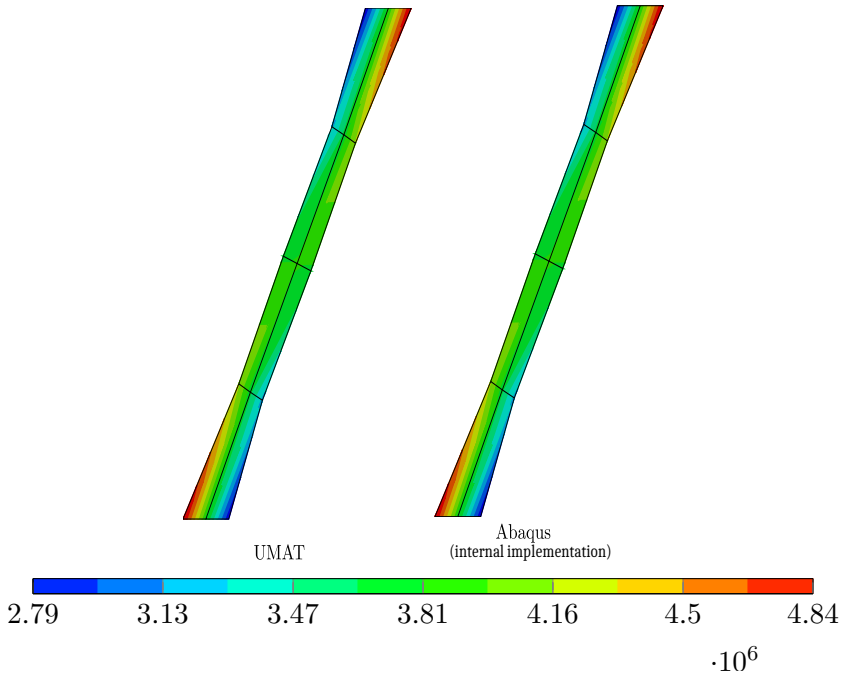

Figure 21: σ_{12} (in Pa) predicted by `UMAT` and the polynomial model from Abaqus.

as well. $\boldsymbol{F}_e \approx \boldsymbol{I} + \boldsymbol{\epsilon}_e$ and $\boldsymbol{C}_e \approx \boldsymbol{I} + 2\boldsymbol{\epsilon}_e$. Similarly, $\lambda_{1e}^2 \approx 1 + 2\epsilon_{1e}$ and $\lambda_{2e}^2 \approx 1 + 2\epsilon_{2e}$. Plane stress conditions are assumed to prevail. Material is taken to be incompressible. In such a case, the stresses in the principal directions in equations 43 and 44 become

$$\tau_A \approx 2C_{10}\left(4\epsilon_A + 2\epsilon_B\right), \tag{101}$$

$$\tau_B \approx 2C_{10}\left(2\epsilon_A + 4\epsilon_B\right). \tag{102}$$

$\dfrac{\partial \psi}{\partial I_1}$ has been approximated by C_{10} for polynomial model. Equation 49 becomes

$$p \approx -4C_{10}\left(\epsilon_A + \epsilon_B\right). \tag{103}$$

Then $\tau_A + p = 4C_{10}\epsilon_A$ and $\tau_B + p = 4C_{10}\epsilon_B$. The evolution equations 50 and 51 become, with $\gamma_0 = 1$,

$$r_1 = \epsilon_{1e} + \frac{\Delta t}{2\eta_D} 4C_{10}\epsilon_{1e} - (\epsilon_{1e})_{tr} = 0 \implies \epsilon_{1e} = \frac{(\epsilon_{1e})_{tr}}{1 + \frac{\Delta t}{\tau}}, \tag{104}$$

$$r_2 = \epsilon_{2e} + \frac{\Delta t}{2\eta_D} 4C_{10}\epsilon_{2e} - (\epsilon_{2e})_{tr} = 0 \implies \epsilon_{2e} = \frac{(\epsilon_{2e})_{tr}}{1 + \frac{\Delta t}{\tau}}, \tag{105}$$

where $\eta_D := 2C_{10}\tau$ has been used. The above equations can be seen to be the backward Euler discretization in time of the PDE

$$\dot{\epsilon}_{Ae} + \frac{\epsilon_{Ae}}{\tau} = \dot{\epsilon}_A. \tag{106}$$

This can be proved by using $\dot{\epsilon}_{Ae} = \frac{\epsilon_{Ae}^n - \epsilon_{Ae}^{n-1}}{\Delta t}$ and $\dot{\epsilon}_A = \frac{\epsilon_A^n - \epsilon_A^{n-1}}{\Delta t}$. Equation 106 then becomes

$$\frac{\epsilon_{Ae}^n - \epsilon_{Ae}^{n-1}}{\Delta t} + \frac{\epsilon_{Ae}^n}{\tau} = \frac{\epsilon_A^n - \epsilon_A^{n-1}}{\Delta t} \implies \epsilon_{Ae}^n = \frac{(\epsilon_{Ae})_{tr}}{1 + \frac{\Delta t}{\tau}}, \tag{107}$$

which is equation 105. In the above equation, $(\epsilon_{Ae})_{tr} = \epsilon_A^n - \epsilon_{Av}^{n-1} = \epsilon_A^n - \left(\epsilon_A^{n-1} - \epsilon_{Ae}^{n-1}\right)$.

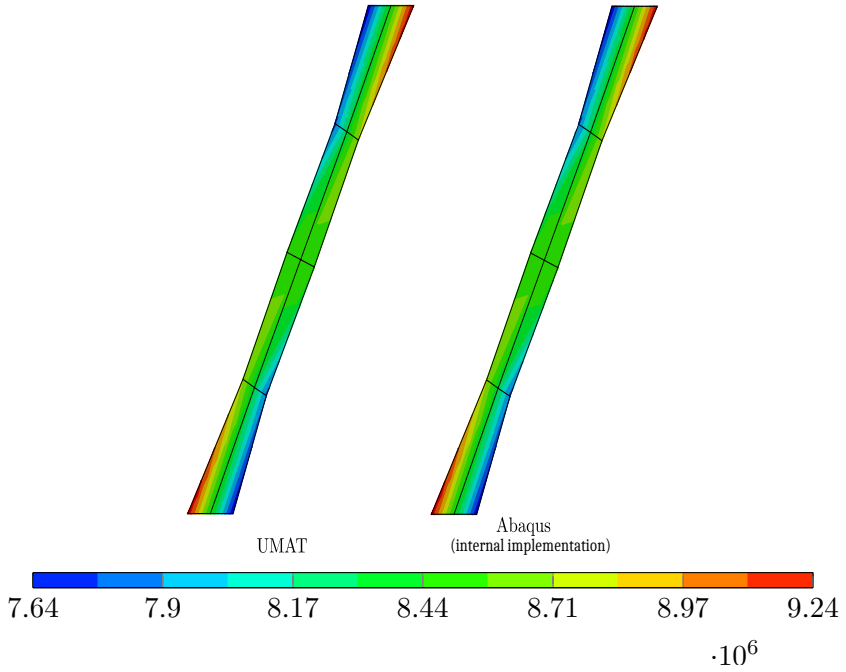

Figure 22: σ_{22} (in Pa) predicted by `UMAT` and the polynomial model from Abaqus.

The FLV model in [14] can be written in the case of small strains and small perturbations by realizing that

$$C^s_{33} = \frac{1}{\det \boldsymbol{C}^s_{2d}} \approx 1, \quad \forall \quad 0 \leq s \leq t, \tag{108}$$

$$(\boldsymbol{C}^s_{2d})^{-1} \approx \boldsymbol{I} - 2\boldsymbol{\epsilon}^s, \quad \forall \quad 0 \leq s \leq t, \tag{109}$$

$$\mathrm{tr}(\hat{\boldsymbol{S}}^s \boldsymbol{C}^s_{2d}) = \mathrm{tr}(\boldsymbol{\tau}^s), \quad \forall \quad 0 \leq s \leq t, \tag{110}$$

$$\hat{\boldsymbol{S}}^s \approx \boldsymbol{\tau}^s \quad \forall \quad 0 \leq s \leq t. \tag{111}$$

Using all the above, the 22 component of Kirchhoff stress can be written as

$$\tau_2 = \int_{-\infty}^{t} g(t-s) \frac{\partial \tau^s_2}{\partial s} \, \mathrm{d}s = \tau^\infty_2 + \tau_{2e}, \tag{112}$$

where τ^∞_2 is the stress in the elastic branch and $\tau_{2e} = 2C_{10}(4\epsilon_{2e} + 2\epsilon_{1e})$ is the stress in the viscous branch, $\epsilon_{2e} = \int_{-\infty}^{t} \exp(-\frac{t-s}{\tau}) \frac{\partial \epsilon_2}{\partial s} \, \mathrm{d}s$. This, in turn, can be seen to be the analytical solution of equation 106. Hence, both FLV and FV models can be seen to give the exactly same result in the limit $\Delta t/\tau \to 0$. However, when $\Delta t/\tau$ does not tend to 0, the two models can result in slightly different result as the FLV model uses the semi-group property of the exponent to integrate the equations while FV model uses backward Euler method.

The predictions of FLV and FV models are examined for the geometry in Fig. 19. The top portion of the model is fixed in the x-direction, $u_x = 0$ and is displaced in y-direction as follows. It is subjected to a displacement of $5\,\mathrm{mm}$ in $5 \times 10^6\,\mathrm{sec}$ to make sure that the viscoelastic effects can be neglected in this step. It is then subjected to a cyclic displacement $A + B\sin(2\pi\omega t)$, where $A = 5\,\mathrm{mm}$, $B = 2\,\mathrm{mm}$, and $\omega = 1000\,\mathrm{s}^{-1}$. The stiffness ratios, g_1 and g_2, for FLV model (with respect to the glassy modulus) have been taken to be 0.3 and 0.4, respectively, while τ_1 and τ_2 to be $1 \times 10^3\,\mathrm{s}$ and $1 \times 10^4\,\mathrm{s}$, respectively. The stiffness ratios ($g_1 = \frac{\psi_1}{\psi_\infty}$ and $g_2 = \frac{\psi_2}{\psi_\infty}$) of FV model (with respect to the rubbery modulus) hence become 1 and 1.33, respectively and the η_Ds are computed as $2C_{10}\tau$. Time step size has been set to $1 \times 10^{-4}\,\mathrm{s}$. Hence, $\frac{\Delta t}{\tau}$ is about 10^{-7}. The evolution of σ_{22} and ϵ_{22} with time for the two models along with the difference between them at the centroid of the element shaded in brown in Fig. 19 can be seen in Fig. 23.

As can be seen, the two models predict the same result to within plotting accuracy. The difference between the stresses predicted by them lies within 3% of the maximum value and the difference between the strains lies within 0.2% of the maximum value. This demonstrates the accuracy of implementation of the FV model into the `UMAT` subroutine.

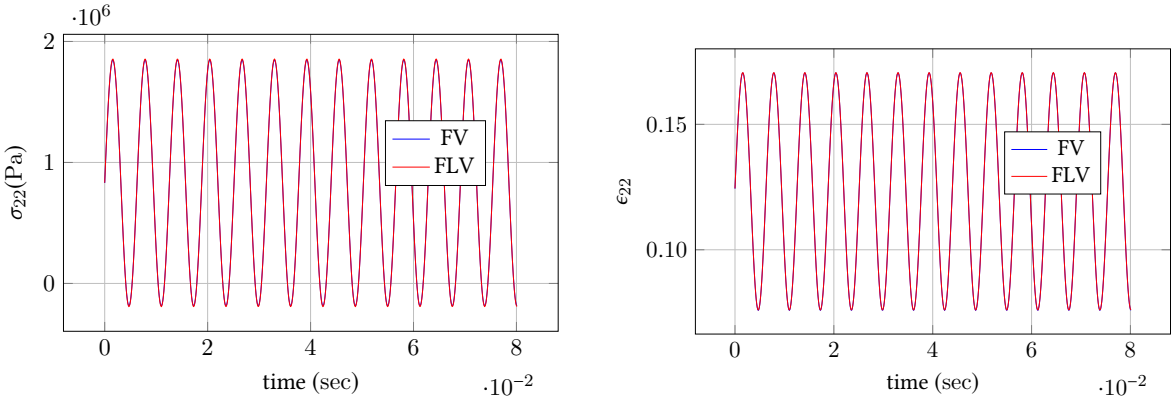

Figure 23: σ_{22} and ϵ_{22} vs time for FLV and FV models. The FLV model has already been implemented within Abaqus while the FV model in the `UMAT`.

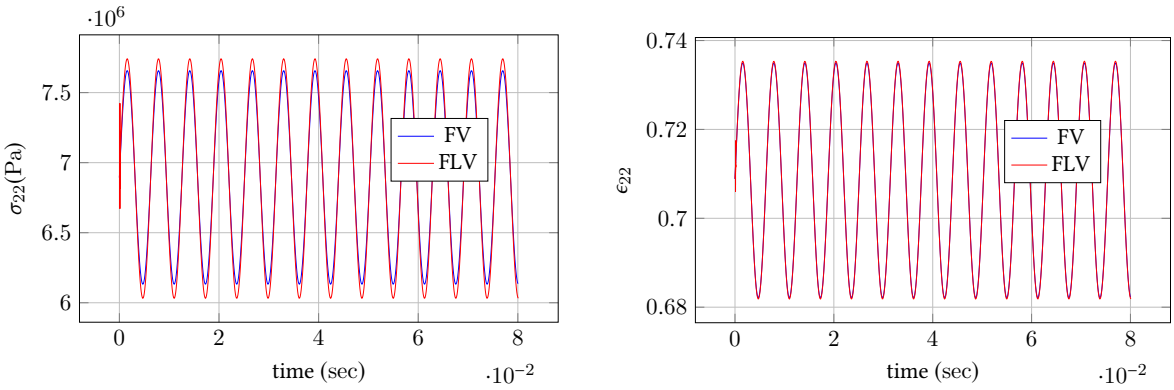

Figure 24: σ_{22} and ϵ_{22} vs time for FLV and FV models.

A.4 Large strains and small perturbations

In this case, the approximations of $\boldsymbol{F}_e$ and $\boldsymbol{C}_e$ in the previous section still hold. However, the background strains are taken to be finite and so, they cannot be approximated using small strain measures. In this case, the evolution equations for FV model for viscous branches remain similar to equation 105, except that the total strains used for the computation of trial strains, ϵ_A, are now logarithmic, $\boldsymbol{\epsilon} = \frac{1}{2}\ln \boldsymbol{C}$. The evolution equations in this case can be shown to be exactly that of [48].

The model in Fig. 19 is again used to test this scenario. The top edge of the model is fixed in the x-direction, $u_x = 0$ and is displaced first vertically by $40\,\mathrm{mm}$ in a span of $5 \times 10^7\,\mathrm{sec}$. It is then subjected to a cyclic displacement $A + B\sin(2\pi\omega t)$, where $A = 40\,\mathrm{mm}$, $B = 2\,\mathrm{mm}$, and $\omega = 1000\,\mathrm{s}^{-1}$. The model coefficients are as in the previous section and the time step has been set to $1 \times 10^{-4}\,\mathrm{s}$ as well.

It can be seen from Fig. 24 that the two models predict slightly different values of stresses at the same strain level. The FV model predicts slightly smaller stress levels than the FLV model. Under large strains and small perturbations, the FV model condenses to the model of Lubliner [48], while the FLV model slightly differs from it (see remark 1.6 of [14]). The slight differences in the predictions between the two models can be attributed to this.